

## Unveiling the Cosmic Chemistry: Revisiting the Mass-Metallicity Relation with JWST/NIRSpec at $4 < z < 10$

ARNAB SARKAR <sup>1</sup>, PRIYANKA CHAKRABORTY <sup>2</sup>, MARK VOGELSBERGER <sup>1</sup>, MICHAEL McDONALD,<sup>1</sup> PAUL TORREY <sup>3</sup>,  
ALEX M. GARCIA <sup>3</sup>, GOURAV KHULLAR,<sup>4</sup> GARY J. FERLAND,<sup>5</sup> WILLIAM FORMAN,<sup>2</sup> SCOTT WOLK,<sup>2</sup>  
BENJAMIN SCHNEIDER,<sup>1</sup> MARK BAUTZ <sup>1</sup>, ERIC MILLER <sup>1</sup>, CATHERINE GRANT <sup>1</sup> AND JOHN ZUHONE<sup>2</sup>

<sup>1</sup>*Kavli Institute for Astrophysics and Space Research, Massachusetts Institute of Technology, 70 Vassar St, Cambridge, MA 02139*

<sup>2</sup>*Center for Astrophysics | Harvard & Smithsonian, 60 Garden St, Cambridge, MA 02138*

<sup>3</sup>*University of Virginia, Virginia, USA*

<sup>4</sup>*University of Pittsburgh, Pittsburgh, PA, 15260*

<sup>5</sup>*University of Kentucky, Lexington, KY*

(Dated: Accepted for publication in ApJ)

### ABSTRACT

We present star formation rates (SFR), the mass-metallicity relation (MZR), and the SFR-dependent MZR across redshifts 4 to 10 using 81 star-forming galaxies observed by the JWST NIRSpec employing both low-resolution PRISM and medium-resolution gratings, including galaxies from the JADES GOODS-N and GOODS-S fields, the JWST-PRIMAL Legacy Survey, and additional galaxies from the literature in Abell 2744, SMACS-0723, RXJ2129, BDF, COSMOS, and MACS1149 fields. These galaxies span a 3 dex stellar mass range of  $10^7 < M_*/M_\odot < 10^{10}$ , with an average SFR of  $7.2 \pm 1.2 M_\odot \text{yr}^{-1}$  and an average metallicity of  $12 + \log(\text{O}/\text{H}) = 7.91 \pm 0.08$ . Our findings align with previous observations up to  $z = 8$  for the MZR and indicate no deviation from local universe FMR up to this redshift. Beyond  $z = 8$ , we observe a significant deviation  $\sim 0.27$  dex) in FMR, consistent with recent JWST findings. We also integrate CEERS (135 galaxies) and JADES (47 galaxies) samples with our data to study metallicity evolution with redshift in a combined sample of 263 galaxies, revealing a decreasing metallicity trend with a slope of  $0.067 \pm 0.013$ , consistent with IllustrisTNG and EAGLE, but contradicts with FIRE simulations. We introduce an empirical mass-metallicity-redshift (MZ- $z$  relation):  $12 + \log(\text{O}/\text{H}) = 6.29 + 0.237 \times \log(M_*/M_\odot) - 0.06 \times (1 + z)$ , which accurately reproduces the observed trends in metallicity with both redshift and stellar mass. This trend underscores the “Grand Challenge” in understanding the factors driving high-redshift galactic metallicity trends, such as inflow, outflow, and AGN/stellar feedback—and emphasizes the need for further investigations with larger samples and enhanced simulations.

*Keywords:* James Webb Space Telescope–High redshift Galaxies–Chemical abundances

### 1. INTRODUCTION

Stellar mass and gas-phase metallicity are two of the most fundamental physical properties of galaxies, serving as key indicators of galaxy evolution. Star formation primarily enhances the metal content of a galaxy, but this enrichment is temporarily offset by the inflow of cosmological gas and large-scale galactic winds, with inflowing gas fueling long-term star formation and outflows

enriching the interstellar medium (ISM) (Davé et al. 2011b; Lilly et al. 2013). The exchange of baryons in and out of galaxies affects their stellar masses ( $M_*$ ), metallicities ( $Z$ ), and star formation rates (SFRs), impacting the mass–metallicity relation (MZR) and the fundamental metallicity relation (FMR;  $M_*$ –SFR– $Z$ ). Therefore, understanding how these quantities evolve with cosmic time and in relation to one another is vital for deciphering the processes that control star formation in galaxies and drive galactic evolution.

The initial evidence of a mass-metallicity relation (MZR) was demonstrated in [Lequeux et al. \(1979\)](#), who found a relationship between total mass and metallicity in irregular and blue compact galaxies. Due to challenges in obtaining reliable galaxy masses, subsequent studies have used optical luminosity as a proxy, showing a clear correlation between blue luminosity and metallicity, with more luminous galaxies exhibiting higher metallicities (e.g., [Garnett & Shields 1987](#); [Zaritsky et al. 1994](#)). The development of reliable stellar population synthesis models ([Bruzual & Charlot 2003](#)) has since enabled more accurate stellar mass measurements from spectral energy distributions (SEDs). In the local Universe, [Tremonti et al. \(2004\)](#) found a tight correlation between galaxy stellar mass and gas-phase oxygen abundance in star-forming galaxies, based on data from  $\sim 53,000$  galaxies in the Sloan Digital Sky Survey (SDSS) early data release ([York et al. 2000](#); [Abazajian et al. 2003](#)). Numerous studies have since identified the mass-metallicity relation in galaxies up to  $z \sim 2.3$  ([Erb et al. 2006a,b](#); [Zahid et al. 2011](#); [Andrews & Martini 2013](#)), demonstrating that the MZR evolves with redshift, showing higher metallicities at lower redshifts for a given stellar mass ([Zahid et al. 2013](#)). [Maiolino et al. \(2008a\)](#) extended the mass-metallicity relation up to  $z \sim 3.5$ , finding that its evolution is much stronger than observed at lower redshifts.

[Mannucci et al. \(2010\)](#) identified an anti-correlation between metallicity and SFR in a large sample of SDSS galaxies, indicating that galaxies of the same stellar mass with higher SFRs tend to have lower gas-phase metallicity, a finding later extended to low-mass galaxies by [Mannucci et al. \(2011\)](#). The observed anti-correlation is attributed to the interplay between the infall of pristine gas, which fuels star formation, and the outflow of enriched material ([Davé et al. 2011a](#); [Dayal et al. 2013](#); [De Rossi et al. 2015](#); [Sánchez et al. 2017](#); [Cresci & Maiolino 2018](#)). This relationship remains largely unevolved between  $z \sim 0$  and  $z \sim 3$  (e.g., [Mannucci et al. 2010](#); [Andrews & Martini 2013](#); [Salim et al. 2014](#); [Cresci et al. 2019](#); [Curti et al. 2020](#); [Sanders et al. 2021](#)), and is therefore referred to as the Fundamental Metallicity Relation (or FMR) (e.g., [Ellison et al. 2008](#); [Lara-López et al. 2010](#)).

In the pre James Webb Space Telescope (JWST) era, accurate measurements of galaxy chemical abundances were limited to redshift  $z = 3.3$  ([Sanders et al. 2021](#)), thereby restricting the study of MZR and FMR for galaxies at higher redshifts. With its wide range of spectroscopic capabilities and unparalleled sensitivity in the near- and mid-infrared band, the JWST and its near-infrared spectrograph NIRSpec ([Ferruit et al.](#)

[2022](#); [Jakobsen et al. 2022](#)) have revolutionized our ability to explore and analyze galaxies from the earliest epochs of the universe. Recently, the use of nebular emission lines and line ratios in star-forming galaxies has proven to be a crucial tool for probing their gas properties, and providing detailed measurements of their metallicities, stellar masses, and star formation rates for galaxies with redshifts up to  $z \sim 10$  ([Shapley et al. 2023](#); [Nakajima et al. 2023](#); [Sanders et al. 2024](#); [Curti et al. 2024](#)) detected through observational campaigns such as the JWST Early Release Observations (JWST-ERO, [Pontoppidan et al. 2022](#)), JWST Advanced Deep Extragalactic Survey (JADES, [Eisenstein et al. 2023](#)), Through the Looking GLASS (GLASS- JWST, [Treu et al. 2022](#)), and the Cosmic Evolution Early Release Science (CEERS, [Finkelstein et al. 2023](#)) programs.

The exceptional capabilities of JWST have allowed us, for the first time, to test whether high-redshift galaxies adhere to the same mass-metallicity-SFR relation as the extensively studied galaxies with redshifts up to  $z \sim 3$ . Using JWST/NIRSpec observations from the Abell 2744 and RXJ-2129 regions, as well as the CEERS survey, [Heintz et al. \(2023\)](#) studied the mass-metallicity relation of galaxies at redshifts  $z = 7-10$ , finding that these high-redshift galaxies have lower gas-phase metallicities compared to local star-forming galaxies at  $z \approx 0$ . Similar findings were reported by [Langeroodi et al. \(2023\)](#), who analyzed a sample of 11 galaxies within the redshift range  $7.2 < z < 9.5$  and provided a quantitative statistical inference of the mass-metallicity relation at  $z \approx 8$ , concluding that galaxies at this epoch are less metal-enriched than those in the local universe.

Using observations from the public spectroscopy programs - ERO, GLASS, and CEERS observed with JWST/NIRSpec, [Nakajima et al. \(2023\)](#) investigated the evolution of the mass-metallicity relation across redshifts  $z = 4-10$ . By analyzing a sample of 135 galaxies, their study revealed that the MZR exhibits only small evolution towards lower metallicity when compared to the well-established relation at  $z \sim 2-3$ . [Curti et al. \(2024\)](#) investigated the metallicity properties of low-mass galaxies within the redshift range  $3 < z < 10$  using deep NIRSpec spectroscopic data from the JADES program, and also found a mild evolution of mass metallicity relation at  $z > 3$  indicating a trend of slightly decreasing metallicity. Similar findings were reported by [Matthee et al. \(2023\)](#), who studied the mass-metallicity relation in galaxies at  $5 < z < 7$  using the first deep JWST/NIRCam wide-field slitless spectroscopic observations, and by [Shapley et al. \(2023\)](#), who examined galaxies at  $2.7 < z < 6.5$  from the CEERS survey, find-

ing no significant evolution in the mass-metallicity relation within that redshift range.

Earlier studies have suggested that the local FMR may not be applicable at redshifts  $z \gtrsim 3.5$  (Troncoso et al. 2014; Onodera et al. 2016). However, many of these studies, based on small sample sizes and predominantly featuring starburst galaxies, do not accurately represent the typical galaxy population at these high redshifts. Interestingly, recent JWST observations have revealed divergence from the local FMR at  $z > 5$  (Heintz et al. 2023; Nakajima et al. 2023; Langeroodi & Hjorth 2023; Curti et al. 2024). Heintz et al. (2023) observed a clear offset in the FMR from that of local galaxies using the same sample of  $7.2 < z < 9.5$  galaxies. Nakajima et al. (2023) found that the FMR remains largely unchanged from  $z = 0$  to  $z = 4-8$ , but exhibits a significant decrease in metallicity at  $z > 8$ . Curti et al. (2024) also reported a deviation in the FMR, finding that high-redshift galaxies exhibit a substantial metal deficiency compared to local galaxies with similar stellar mass and star formation rate. The origins of these offsets remain ambiguous, potentially indicating either authentic deviations from the FMR, systematic inaccuracies in metallicity determinations, or limitations inherent to current observational methodologies. The limited sample size used within individual studies, particularly in the  $z = 8-10$  range, undoubtedly contributes to this ambiguity.

In this paper, we investigate the mass-metallicity-SFR relations and their evolution across redshifts for a sample of 81 star-forming galaxies ranging from redshifts  $4 < z < 10$ , utilizing observations from the NIRSPEC instrument, employing both its low-resolution *PRISM* and medium-resolution grating capabilities. Our dataset includes:

- 54 galaxies from the GOODS-S and GOODS-N fields, part of the JADES public data release 3 (D’Eugenio et al. 2024).
- 22 galaxies as reported in JWST-PRIMAL Legacy Survey (Heintz et al. 2024).
- 5 galaxies selected from various fields as reported in literature: Abell 2744, BDF, COSMOS (Venturi et al. 2024), RXJ2129 (Wang et al. 2024), and MACS1149 Marconcini et al. (2024).

This sample of galaxies, previously never utilized for studying the SFR-MZR, provides a novel and independent dataset for investigating the SFR-MZR at high redshifts. This allows us to not only compare and contrast our findings with previous studies and simulations but also to offer independent constraints on MZR and FMR

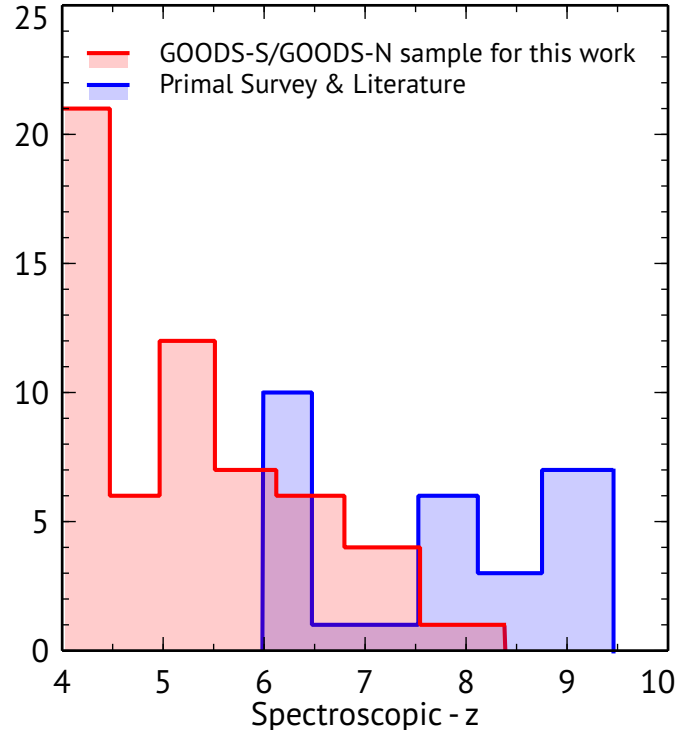


**Figure 1.** Redshift distribution of the galaxies selected for the analysis of stellar mass-metallicity-SFR correlations. The red histogram shows the redshift distribution of galaxies from the GOODS-N and GOODS-S Data Release 3 (D’Eugenio et al. 2024), whereas the blue histogram represents the distribution of galaxies from the PRIMAL survey (Heintz et al. 2024), supplemented with additional samples from the literature (e.g., Venturi et al. 2024; Wang et al. 2024; Marconcini et al. 2024).

(e.g., Vogelsberger et al. 2014a, 2020; Diemer et al. 2018, 2019). Details on these galaxies are provided in Table 2, 3, 4, and 5 in Appendix, their distribution across redshifts is depicted in Figure 1. The organisation of the paper is as follows. In Section 2, we discussed data analysis and methods involved in fitting *PRISM* and grating spectrum. In Section 4, we present the physical properties of our galaxy sample, including emission line-flux ratios, AGN contamination removal, metallicity measurements, and mass-metallicity relation. In Section 5 and 6, we discuss the mass-metallicity relation and the fundamental metallicity relation and their evolution. In Section 7, we probe the evolution of metallicity with redshift and MZ- $z$  relation. In Section 8, we summarize our findings.

Throughout this paper, we adopt the AB magnitude system (Oke & Gunn 1983) and cosmological parameters reported by Planck Collaboration et al. (2020): the Hubble constant  $H_0 = 67.4 \text{ km s}^{-1} \text{ Mpc}^{-1}$ , matter den-

sity parameter  $\Omega_M = 0.315$ , and dark energy density  $\Omega_\Lambda = 0.685$ .

## 2. OBSERVATIONS AND METHODS

For this work, we assemble a sample of 81 galaxies in redshift range  $4 < z < 10$  primarily derived from publicly available programs or data releases, such as JADES (data release 3; e.g., D’Eugenio et al. 2024; Robertson 2022; Eisenstein et al. 2023; Bunker et al. 2023; Curtis-Lake et al. 2023), JWST-PRIMAL Legacy Survey (Heintz et al. 2024), and from literature (e.g, Venturi et al. 2024; Wang et al. 2024; Marconcini et al. 2024). We select these galaxies based on below criteria:

- Spectra are obtained through the application of the NIRSpec low-resolution configuration *PRISM/CLEAR*, covering the spectral range of  $0.6\text{--}5.3\mu\text{m}$ , and medium resolution gratings ( $R\sim 1000$ ), including G140M/F070LP ( $0.7\text{--}1.27\mu\text{m}$ ), G235M/F170LP ( $1.66\text{--}3.07\mu\text{m}$ ), and G395M/F290LP ( $2.87\text{--}5.10\mu\text{m}$ ).
- The minimum signal-to-noise ratios should be  $\geq 3$  for faint lines (such as  $H\gamma$ ,  $[\text{N II}]\lambda 6584$ , and  $[\text{S II}]\lambda\lambda 6716, 31$ ) and  $\geq 5$  for bright lines (such as  $[\text{O III}]\lambda\lambda 5007, 4959$ ,  $H\alpha$ , and  $H\beta$ ).
- For each galaxy,  $[\text{O III}]\lambda\lambda 5007$  and  $H\beta$  should be present with required signal-to-noise ratio, as well as one of below emission line or pairs should be present  $[\text{O II}]\lambda\lambda 3727, 29$ ,  $[\text{N II}]\lambda 6584$  &  $H\alpha$ , and  $[\text{S II}]\lambda\lambda 6716, 31$  &  $H\alpha$ .
- These galaxies should be star-forming galaxies. Mass-Excitation diagnostic has been utilized to identify star-forming galaxies from AGN, as discussed in Section 4.2.

If medium-resolution grating spectra are unavailable or do not cover the spectral range needed to capture three key emission lines-  $H\beta$ ,  $[\text{O II}]\lambda 3727, 29$ ,  $[\text{O III}]\lambda\lambda 5007, 4959$ - we instead utilize low-resolution *PRISM* spectra. Out of 81 galaxies in our study, 67 have spectra observed with both *PRISM* and medium-resolution gratings. However, 9 galaxies lack medium-resolution grating spectra. For most of the galaxies, we utilize multi-object spectroscopy observations using the micro-shutter assembly (MSA) of NIRSpec on-board JWST (Ferruit et al. 2022). During these observations, three micro-shutters were activated for each target. An exposure protocol was employed consisting of a three-point nodding sequence along the slit, ensuring comprehensive coverage and improved data quality for each target. For each JADES GOODS-S and GOODS-N targets,

the flux-calibrated 1D and 2D spectra were produced by the JADES team using a custom pipeline developed by the ESA NIRSpec Science Operations Team (SOT) and Guaranteed Time Observations (GTO) teams. For detailed descriptions of the data reduction steps and methods, we refer readers to Bunker et al. (2023), Curti et al. (2024), D’Eugenio et al. (2024) and references therein. For this paper, we adopted the reduced and flux-calibrated *medium-tier* 1D and 2D spectra of hundreds of targets, which were released publicly as part of JADES Data Release 3<sup>1</sup> (D’Eugenio et al. 2024).

For targets selected from the JWST-PRIMAL Legacy Survey, we utilized DAWN JWST Archive (DJA), containing reduced images, photometric catalogs, and spectroscopic data for public JWST data products<sup>2 3</sup>. The DJA spectroscopic archive (DJA-Spec) includes observations from major programs such as CEERS (Finkelstein et al. 2022), GLASS-DDT (Treu et al. 2022), JADES (Bunker et al. 2023), and UNCOVER (Bezanson et al. 2022). For detailed data reduction processes we refer readers to Heintz et al. (2024).

Additionally, we selected 5 galaxies from the literature, including three galaxies located in the Abell 2744, BDF, and COSMOS fields with redshifts of 7.89, 7.11, and 6.36, respectively (Venturi et al. 2024). The other two galaxies, at redshifts 8.16 and 9.11, were observed in the RXJ2129 and MACS1149 galaxy cluster fields, as reported by Wang et al. (2024) and Marconcini et al. (2024), respectively. For these 5 galaxies, we utilized the redshift, stellar mass,  $H\beta$  flux, and metallicity measurements reported in their respective studies.

## 3. SPECTRAL FITTING

We discuss the detailed spectral fitting processes below.

### 3.1. *PRISM/CLEAR* spectra

To measure the stellar mass and spectral energy distribution (SED)-based redshift of each targets, we fitted the *PRISM* spectra by using the SED fitting code BAGPIPES (Carnall et al. 2018). BAGPIPES creates detailed model galaxy spectra and fits them to photometric and spectroscopic observations (Feroz & Hobson 2008). This method produces posterior distributions of galaxy properties for each source in the sample. BAGPIPES is versatile, capable of modeling galaxies with various star formation histories (SFHs), including delayed- $\tau$ , con-

<sup>1</sup> <https://jades-survey.github.io/scientists/data.html>

<sup>2</sup> <https://dawn-cph.github.io/dja>

<sup>3</sup> [https://s3.amazonaws.com/msaexp-nirspec/extractions/nirspec\\_graded\\_v2.html](https://s3.amazonaws.com/msaexp-nirspec/extractions/nirspec_graded_v2.html)

stant, and bursts (e.g., Lower et al. 2020; Chakraborty et al. 2024).

For this study, we used a constant star-formation model with the minimum and maximum star formation ages were allowed to vary between 0 and 2 Gyr. We adopted stellar population synthesis models based on the 2016 version of the BC03 models (Bruzual & Charlot 2003). These models assume the initial mass function (IMF) from Kroupa (2002) and include nebular line and continuum emissions using CLOUDY (Chatzikos et al. 2023). The SED-fitting was conducted over a broad range of parameters, with stellar mass  $\log(M_*/M_\odot)$  varying between 4 and 13, and stellar metallicities  $\log(Z/Z_\odot)$  ranging from 0.005 to 2.5. BAGPIPES assumes the solar abundances from Anders & Grevesse (1989) and incorporates ISM depletion factors and He and N scaling relations from Dopita et al. (2000).

The ionization parameter for nebular line and continuum emissions was varied between  $-4$  and  $-1$ . We adopted the Calzetti dust attenuation curve (Calzetti et al. 2000) with an extinction parameter  $A_V$  ranging from 0 to 4. Additionally, to address birth-cloud dust attenuation, we introduced a multiplicative factor ( $1 < \eta < 2$ ) to the dust model. This accounts for the increased dust attenuation typically observed around H II regions, which is usually double that of the general ISM within the galaxy’s first 10 Myr (Bunker et al. 2023). To model this effect, we set the maximum age of the birth-cloud to 0.01 Gyr (Bunker et al. 2023).

We note that the spectral resolution of the *PRISM* spectra varies significantly with wavelength, ranging from  $R \sim 30$  at  $1.2\mu\text{m}$  to a peak of  $R \sim 300$  at the cutoff wavelength of  $5\mu\text{m}$ . Since we only use the *PRISM* spectra to estimate the stellar mass and SED-based redshift, we chose not to fit these spectra with variable resolution settings in BAGPIPES. This simplifies our analysis and avoids the systematics that come with adjusting the resolution settings for different wavelengths. Instead, we focused on extracting reliable stellar mass and SED-based redshift estimates. The uncertainties on best-fit parameters are derived from the posterior distribution of each parameter. The resulting best-fit stellar masses for our sample of galaxies are listed in Table 2, 3, 4, and 5 in Appendix.

### 3.2. Emission line flux measurement

We conduct measurements of emission-line fluxes for each target using publicly released 1D medium-resolution grating spectra obtained through G140M/F070LP, G235M/F170LP, and G395M/F290LP dispersers/filters. For 9 galaxies, medium-resolution grating spectra are unavailable; therefore, we use

*PRISM* spectra to measure emission-line fluxes. Our analysis focused on extracting crucial emission lines, including hydrogen Balmer lines, [O II] $\lambda\lambda$ 3727,29, [O III] $\lambda\lambda$ 5007,4959, [N II] $\lambda$ 6584, and [S II] $\lambda\lambda$ 6716,31. For each emission line, we applied Gaussian profile fitting to accurately determine their fluxes. The errors associated with these flux measurements were computed by combining noise levels from spectral bins within the Full Width at Half Maximum (FWHM) centered on the Gaussian peak, providing robust estimates of measurement uncertainties. In low-resolution *PRISM* spectra, the doublet lines are typically blended, such as [O II] $\lambda\lambda$ 3727,29 and [O III] $\lambda\lambda$ 5007,4959. Consequently, we use a single Gaussian profile to represent each of the [O II] and [O III] blend. To estimate the [O III] $\lambda$ 5007 line-flux, we assume a theoretical flux ratio of 2.98 for the [O III] $\lambda\lambda$ 5007,4959 doublet (Storey & Zeppen 2000).

To evaluate the quality of our measurements, we calculate the signal-to-noise ratios (S/N) for each emission line. We establish a minimum S/N criterion of  $\geq 3\sigma$  for including a given emission line in our subsequent metallicity calculations. Specifically, our sample selection criteria required galaxies to exhibit detectable H $\beta$  and [O III], in addition to having at least one emission line—[O II] $\lambda\lambda$ 3727,29, [N II] $\lambda$ 6584, or [S II] $\lambda\lambda$ 6716,31—measured at or above the  $3\sigma$  confidence level. This methodical approach enable us to robustly measure and validate emission-line fluxes across our sample, ensuring that only reliable data points are utilized in deriving the gas-phase metallicities of galaxies at high redshifts.

## 4. DETERMINING THE PHYSICAL PROPERTIES OF GALAXIES

### 4.1. Dust corrections and Line ratios

Our primary objective in this study is to measure SFR and gas-phase metallicity of galaxies at high redshifts, which are significantly impacted by the dust reddening. To achieve accurate measurements, we carefully accounted for the corrections due to dust reddening on the key emission lines before using their fluxes for further analysis. Based on the empirical extinction relationship established by Calzetti et al. (1994), the intrinsic luminosities (dust-corrected),  $L_{\text{int}}$  of the emission lines, can be estimated using

$$L_{\text{int}}(\lambda) = L_{\text{obs}}(\lambda)10^{0.4k(\lambda)E(B-V)}, \quad (1)$$

where,  $L_{\text{obs}}(\lambda)$  represents the observed luminosities,  $k_\lambda$  denotes the extinction coefficient at wavelength  $\lambda$ , and the specific reddening curve  $k_\lambda$  was adopted from Calzetti et al. (2000).

We use three different approaches to determine the dust-corrected flux:

- For galaxies at  $z < 6.75$ , where both  $H\alpha$  and  $H\beta$  are detected with a  $S/N \geq 3$ , we estimate  $E(B-V)$  using the Balmer decrement method. We assume an intrinsic flux ratio of  $H\alpha/H\beta = 2.86$  (Osterbrock & Ferland 2006) and apply the dust extinction curve from Calzetti et al. (2000).
- For galaxies at  $z \geq 6.75$ , where  $H\alpha$  is not observable due to the spectral coverage of NIRSpec, we instead use the  $H\gamma/H\beta$  ratio with an assumed intrinsic value of  $H\gamma/H\beta = 0.47$ , corresponding to a temperature of  $10^4$  K for Case B recombination (Osterbrock & Ferland 2006).
- If neither  $H\gamma$  nor  $H\alpha$  is detected, we estimate the nebular dust attenuation using SED fitting performed on *PRISM* spectra using the BAGPIPES code, which incorporates a two-component dust attenuation model for both nebular and stellar emission (see Section 3.1).

We analyze gas-phase metallicity using line ratio diagnostics, as described in Section 4.4. We calculate line flux ratios using dust-corrected emission lines: [O II] $\lambda\lambda 3727, 29$ , [O III] $\lambda\lambda 5007, 4959$ , [N II] $\lambda 6584$ , and [S II] $\lambda\lambda 6716, 31$ . For inclusion in our analysis, each line ratio requires all constituent lines to be detected with a significance of at least  $3\sigma$ . Specifically, we consider the following line ratios: R3, O32, N2, and S2.

$$R3 = \frac{[\text{O III}]\lambda 5007}{H\beta} \quad (2)$$

$$O32 = \frac{[\text{O III}]\lambda 5007}{[\text{O II}]\lambda\lambda 3727, 29} \quad (3)$$

$$N2 = \frac{[\text{N II}]\lambda 6584}{H\alpha} \quad (4)$$

$$S2 = \frac{[\text{S II}]\lambda\lambda 6717, 31}{H\alpha} \quad (5)$$

Given the close proximity of the involved lines, the N2 ratios are largely unaffected by reddening correction. In contrast, O32 and S2 ratios are sensitive to reddening. Additionally, R3 ratio is slightly sensitive to reddening due to the narrow separation of the lines involved.

#### 4.2. AGN contamination and star-forming galaxies

In this study, we utilize line-flux ratio diagnostics specifically developed for measuring gas-phase metallicity in star-forming regions and galaxies. However,

ionization driven by AGNs can compromise these standard metallicity calibrations by introducing inaccuracies if AGN emissions contaminate the emission line-fluxes. To ensure the accuracy of our metallicity assessments, we meticulously scrutinize each galaxies for potential AGN contamination. We have adopted two methods to systematically exclude AGN contamination from our sample, thereby enhancing the reliability of our findings.

First, we use the Mass-Excitation (MEx) diagnostic diagrams, as introduced by Juneau et al. (2014) and refined by Coil et al. (2015), which utilize [O III] $\lambda 5007/H\beta$  (R3) emission-line ratio with stellar mass for distinguishing between AGNs and star-forming galaxies. This diagram serves as an alternative to the widely used BPT diagram (e.g., Baldwin et al. 1981; Kewley et al. 2013), which compares the [O III] $\lambda 5007/H\beta$  to the [N II] $\lambda 6584/H\alpha$  emission line ratios, especially when the [N II] or  $H\alpha$  lines fall out of the visibility window, or are blended. Since we solely measure emission-line fluxes from the medium-resolution grating spectra, we, therefore, use dust-corrected [O III] $\lambda 5007$  and  $H\beta$  fluxes for the MEx diagram. Figure 2 presents our JWST samples in the  $\log([\text{O III}]\lambda 5007/H\beta) - \log(M_*/M_\odot)$  plane.

In Figure 2, the blue and red curves indicate steep gradients at  $P(\text{AGN}) \sim 0.3$  and  $P(\text{AGN}) \sim 0.8$ , respectively. These curves represent the probability that a galaxy hosts an AGN, established by Coil et al. (2015) for  $z = 2.3$  galaxies and AGN from the MOSDEF survey (He et al. 2024). The positions of our sources in the MEx diagram suggest that our sample predominantly comprises star-forming galaxies, positioned below or close to the boundary line. Consequently, no possible AGN is eliminated and we retain all galaxies in our sample. Similar approach is also adopted by He et al. (2024) to distinguish star-forming galaxies from AGN in GLASS-JWST sample of galaxies. Additionally, we visually inspected spectra for each galaxies to search for evidence of broad emission line regions (Sarkar et al. 2021).

#### 4.3. Star formation rate for high redshift galaxies

The relationship between stellar mass and SFR exhibits a tight correlation across the redshift range  $z \sim 0 - 2$ , characterized by a slope slightly below unity and a scatter generally under 0.3 dex (Noeske et al. 2007; Elbaz et al. 2007; Daddi et al. 2007). This correlation between stellar mass and SFR in star-forming galaxies is commonly referred to as the galaxy main sequence (MS). However, results for higher redshift galaxies ( $z > 2$ ) have shown considerable divergence in the literature (Speagle et al. 2014).

While many studies suggest a tight correlation at higher redshifts (Pannella et al. 2009; Magdis et al. 2010;

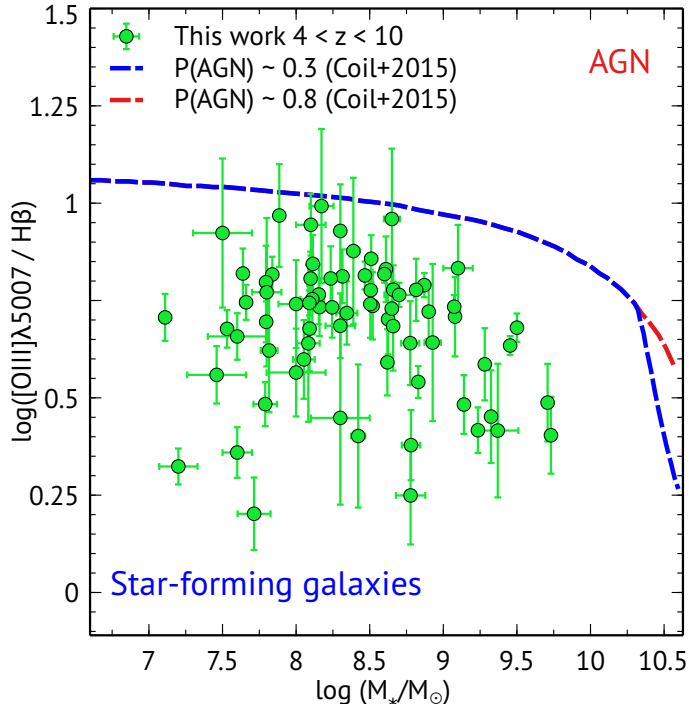


**Figure 2.** The Mass-Excitation (MEx) diagnostic for our full sample, plotting the  $\log([\text{O III}]\lambda 5007 / \text{H}\beta)$  against the  $\log$  of stellar mass. This diagnostic is adapted from He et al. (2024), with the MEx curves originally established by Coil et al. (2015). The locations of probable AGN galaxies, with likelihoods of  $\sim 0.3$  and  $\sim 0.8$  are indicated by the blue and red curves, respectively. We find no significant AGN contamination in our sample.

Lee et al. 2011; Steinhardt et al. 2014), implying smooth gas accretion and aligning well with hydrodynamic simulations (Finlator et al. 2006; Davé 2008), other studies find no correlation or high scatter in the SFR–stellar mass relationship (Reddy et al. 2006; Lee et al. 2012), hinting towards bursty star formation. This ambiguity is compounded by the significant challenges in establishing the correlation at high redshifts, due to various systematic uncertainties and selection effects inherent in compiling representative galaxy samples (e.g., Grazian et al. 2015; Förster Schreiber & Wuyts 2020; Furtak et al. 2021).

For this work, we use  $\text{H}\beta$  as an SFR tracer in lieu of the commonly used  $\text{H}\alpha$  luminosity, as it is the best indicator for ongoing ( $\sim 10$  Myr) star formation activity (e.g., Heintz et al. 2023; Nakajima et al. 2023). This choice is also necessitated by the spectral coverage limitations of NIRSpect, which do not extend to  $\text{H}\alpha$  at redshifts  $z > 6.75$ . The use of  $\text{H}\beta$  allows us to maintain consistency in SFR measurements across our sample. The SFR is derived based on  $\text{H}\beta$  luminosity assuming a

Kroupa IMF (Kroupa 2002) as (Heintz et al. 2023)

$$\text{SFR}_{\text{H}\beta} (M_{\odot} \text{yr}^{-1}) = 5.5 \times 10^{-42} L_{\text{H}\beta} (\text{erg/s}) \times f_{\text{H}\alpha/\text{H}\beta}, \quad (6)$$

where  $f_{\text{H}\alpha/\text{H}\beta} = 2.86$  is theoretical flux ratio between  $\text{H}\alpha$  and  $\text{H}\beta$  assuming a Case B recombination model at  $T_e = 10^4$  K (Osterbrock & Ferland 2006). Figure 3 illustrates correlation between stellar mass and SFR for our entire sample of 81 galaxies, spanning redshifts from  $z = 4$  to 10. The stellar mass is derived from the BAGPIPES fit, as discussed in Section 3.1. The SFR and stellar masses of our sample is listed in Table 2, 3, 4, and 5 in Appendix.

Early results from the CEERS/NIRCam-selected galaxies indicate that the increasing trend of the SFR– $M_{\star}$  relation persists at least out to  $z = 8 - 9$  (Fujimoto et al. 2023). This trend aligns with predictions from simulations, which attribute it to the increased gas accretion rate onto dark matter halos at higher redshifts (Behroozi et al. 2013). We contextualize our findings by comparing them with datasets from several earlier surveys. This includes the JADES/NIRSpect surveys for galaxies within the redshift range  $z = 3 - 10$  (Curti et al. 2024), the CEERS/NIRSpect survey focusing on galaxies at  $z = 4 - 10$  (Nakajima et al. 2023). Additionally, we compare our results with the main sequence of star-forming galaxies at  $z \sim 6$ , as documented in Salmon et al. (2015) and Popesso et al. (2023), as well as at  $z \sim 0$  (Speagle et al. 2014).

Despite large scatter, our results demonstrate a upward trend in SFR as stellar mass increases (Spearman coefficient of 0.4), consistent with the previous studies. The galaxies in our sample exhibit a distribution along the sequence of specific star formation rates (sSFR) ranging from  $10^{-9}$  to  $10^{-7} \text{ yr}^{-1}$ . This distribution aligns well with the star formation main sequence observed in galaxies at  $z = 4 - 7$ , where typical sSFR values are between  $10^{-8.5}$  and  $10^{-6.5} \text{ yr}^{-1}$  (Stark et al. 2013; Santini et al. 2017; Nakajima et al. 2023).

#### 4.4. Gas-phase Metallicity

We next estimate the gas-phase metallicities for individual galaxies in our sample. We use reddening-corrected emission line-fluxes obtained from medium resolution gratings to determine the gas-phase metallicity (Kewley et al. 2019). There are two widely-used methods to determining the gas-phase metallicity: (1) direct  $T_e$ -based method, which involves accurate flux measurements of few key emission lines, such as  $[\text{O II}]\lambda 4363$  (Sanders et al. 2024), (2) empirical method, which involves comparing line-ratios to empirical calibrations, constructed using samples for which metallicity has been derived using “direct method” (e.g., Curti

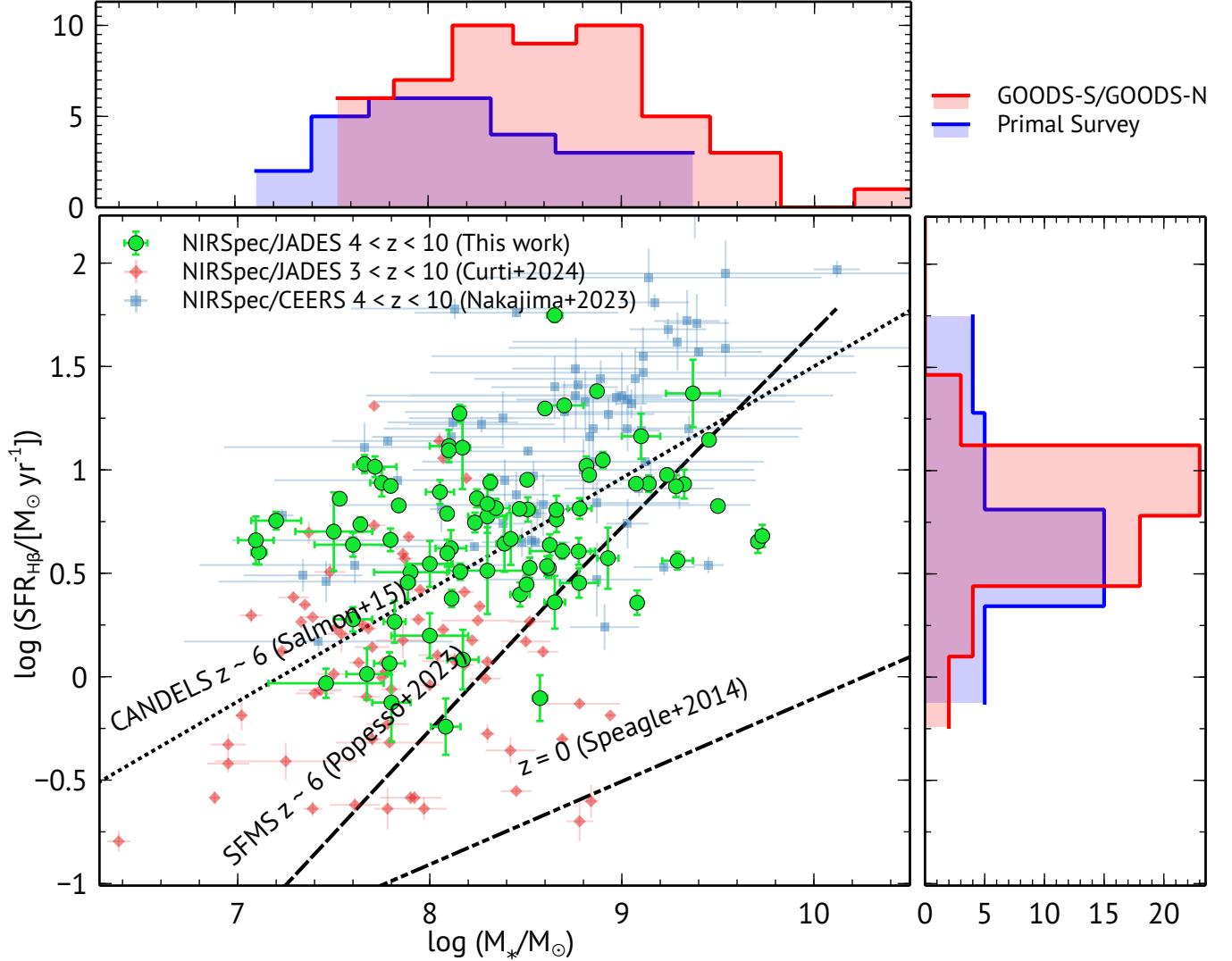


**Figure 3.** Stellar mass versus star formation rate for our full sample of galaxies within the redshift range  $4 < z < 10$  utilized in this study (green data points). The top and side panels respectively display histograms of stellar mass and SFR distributions. The red histogram represents data from GOODS-N and GOODS-S Data Release 3, while the blue histogram combines data from the PRIMAL survey (Heintz et al. 2024) with additional high-redshift galaxies from the literature. We also compared this distribution with prior high-redshift studies: the NIRSpec/CEERS survey for  $4 < z < 10$  galaxies (Nakajima et al. 2023), the NIRSpec/JADES survey for  $3 < z < 10$  galaxies (Curti et al. 2024). The main sequence star formation rates from the CANDELS survey at  $z \sim 6$  galaxies (Salmon et al. 2015), star-forming galaxies (SFGs) at  $z \sim 6$  (Popesso et al. 2023), and studies of the local universe at  $z \sim 0$  (Speagle et al. 2014). The plotted data points from Nakajima et al. (2023) and Curti et al. (2024) are based on  $H\alpha(H\beta)$  derived SFRs, originally calibrated for a Chabrier (2003) IMF. For consistency with our analysis, we have scaled these SFRs to match the Kroupa (2002) IMF used in this study, using a scaling factor of 1.06 from Madau & Dickinson (2014).

et al. 2020; Nakajima et al. 2023). Several previous studies presented empirical calibrations, such as, Pettini & Pagel (2004); Maiolino et al. (2008a); Marino et al. (2013); Curti et al. (2017); Bian et al. (2018); Curti et al. (2020); Nakajima et al. (2022); Sanders et al. (2024)

For this paper, we adopt the revisited calibrations derived by Curti et al. (2020) and later compared with the calibrations by Nakajima et al. (2022). Both of these calibrators are widely used to measure the met-

allcity at high-redshift galaxies (e.g., Curti et al. 2024; Venturi et al. 2024). Their methodology involved utilizing the largest sample of extremely metal-poor galaxies (EMPGs) and stacking a sample of SDSS galaxies to accurately measure metallicity based entirely on the reliable measurements of the direct  $T_e$  method.

We primarily use R3 index for measuring metallicity for individual galaxies. A limitation of using R3 index as a metallicity callibrator is that it can yield two differ-

ent metallicity estimates for the same R3 value (Curti et al. 2020; Lequeux et al. 1979; Sanders et al. 2024). If the metallicities obtained from the R3 index are close, typically occurring around the peak value near  $12 + \log(\text{O}/\text{H}) = 8.0$ , we adopt the  $1\sigma$  lower limit from the low-metallicity solution as the lower bound and the  $1\sigma$  upper limit from the high-metallicity solution as the upper bound, following the approach in Nakajima et al. (2023). When encountering two well-separated metallicity solutions, we utilize the O32 index to differentiate between the degenerate values of metallicities. If the  $[\text{O II}]\lambda\lambda 3727, 29$  line is not detected with  $\geq 3\sigma$  level, it is not possible to calculate the O32 index, we instead utilize the N2 and S2 indices to break the degeneracy whenever available. Similar methods for breaking the degeneracy between two metallicity solutions has been adopted by Nakajima et al. (2023) and Curti et al. (2024).

An alternative technique involves using the equivalent width of  $\text{H}\beta$  ( $\text{EW}(\text{H}\beta)$ ) to estimate O32 when  $[\text{O II}]\lambda\lambda 3727, 29$  is not detected at a  $3\sigma$  level, based on the average relationship identified by Nakajima et al. (2022). This method can help resolve the metallicity degeneracy stemming from the R3 calibration. However, we chose not to employ this technique in this work to avoid introducing potential systematic uncertainties in our metallicity measurements. For galaxies where we could not observationally determine O32, N2, or S2 due to a non-detection of one or more of the lines involved at  $3\sigma$  level, we left the metallicities for those galaxies unconstrained and excluded them from our final sample. Our final data set for analyzing the MZR includes a total of 81 star-forming galaxies, comprising 54 galaxies from the GOODS-S and GOODS-N fields, 22 galaxies reported in the JWST Primal Survey, and an additional 5 galaxies selected from the literature. Metallicities of our sample of galaxies are listed in Table 2, 3, 4, and 5 in Appendix.

## 5. THE MASS-METALLICITY RELATION

One of the primary objectives of this paper is to study the evolution of metallicity in star-forming galaxies. In this section, we present the stellar mass-metallicity relation (or MZR) at the high-redshift using our final sample of galaxies. Specifically, we use the metallicity measurements steps discussed in Section 4.4 and the stellar mass measurements derived from the BAGPIPES fit (Section 3.1) to probe the MZR. Figure 4 illustrates our sample of galaxies in the stellar mass-metallicity plane. Sanders et al. (2021) showed that the average MZR can be approximated as

$$12 + \log(\text{O}/\text{H}) = \gamma \times \log\left(\frac{M_\star}{10^{10}M_\odot}\right) + Z_{10} \quad (7)$$

**Table 1.** Comparing MZR with different studies following equation 7.  $Z_8$  is converted to  $Z_{10}$  using  $Z_{10} = 2\gamma + Z_8$ .

Study	$z$ range	$\gamma$	$Z_{10}$
This work	4–10	$0.27 \pm 0.02$	$8.28 \pm 0.08$
	4–6	$0.28 \pm 0.03$	$8.37 \pm 0.13$
	6–8	$0.23 \pm 0.04$	$8.29 \pm 0.18$
	8–10	$0.21 \pm 0.04$	$8.09 \pm 0.11$
Nakajima et al. (2023)	4–10	$0.25 \pm 0.03$	$8.24 \pm 0.05$
Curti et al. (2023)	3–10	$0.17 \pm 0.03$	$8.06 \pm 0.18$
	3–6	$0.18 \pm 0.03$	$8.11 \pm 0.17$
	6–10	$0.18 \pm 0.03$	$7.87 \pm 0.45$
Sanders et al. (2021)	0	$0.28 \pm 0.01$	$8.77 \pm 0.01$
	2.3	$0.30 \pm 0.02$	$8.51 \pm 0.02$
	3.3	$0.29 \pm 0.02$	$8.41 \pm 0.03$
Li et al. (2023)	2	$0.16 \pm 0.02$	$8.50 \pm 0.13$
	3	$0.16 \pm 0.01$	$8.40 \pm 0.06$
Heintz et al. (2023)	7–10	0.33	7.95
He et al. (2024)	1.9	$0.23 \pm 0.03$	$8.54 \pm 0.12$
	2.88	$0.26 \pm 0.04$	$8.57 \pm 0.15$

where the slope  $\gamma$  and offset  $Z_{10}$  (the gas-phase metallicity at a stellar mass of  $10^{10}M_\odot$ ) can be estimated by fitting to observed MZR.

We divide our full sample ( $4 < z < 10$ ) into three stellar mass ranges:  $M_\star = 10^7 - 10^8$ ,  $10^8 - 10^9$ , and  $10^9 - 10^{10}$  solar masses. In Figure 4, these average points are represented by large red circles. For our full sample, we determine the best-fit slope of  $\gamma = 0.27 \pm 0.02$  and metallicity intercept  $Z_{10} = 8.28 \pm 0.08$ . The best-fit regression line, along with its  $1\sigma$  uncertainty, is shown in Figure 4. We next compare our results with that of previous studies of the MZR at lower redshifts. Specifically, Curti et al. (2020), who analyzed SDSS galaxies in the local universe using a set of strong-line diagnostics calibrated on a fully  $T_e$ -based abundance scale, covering the full range of stellar mass and star formation rates spanned by SDSS galaxies. Additionally, we compare our MZR findings with those of Sanders et al. (2021), who investigated the MZR for galaxies over the range  $z = 0 - 3.3$ , utilizing samples of approximately 300 galaxies at  $z \sim 2.3$  and 150 galaxies at  $z \sim 3.3$  from the MOSDEF survey. Furthermore, we compare our results with the MZR obtained by Li et al. (2023) for a sample of 51 dwarf galaxies at  $z = 2 - 3$ , using Near-Infrared Imager and Slitless Spectrograph (NIRISS) grism spectroscopy from JWST observations in the A2744 and SMACS J0723-3732 fields. Table 1 shows the comparison of  $\gamma$  and  $Z_{10}$  with that of several previous works. The best-fit slope and normalizations of our sample of galaxies are consistent with that of high-redshift CEERS galaxies

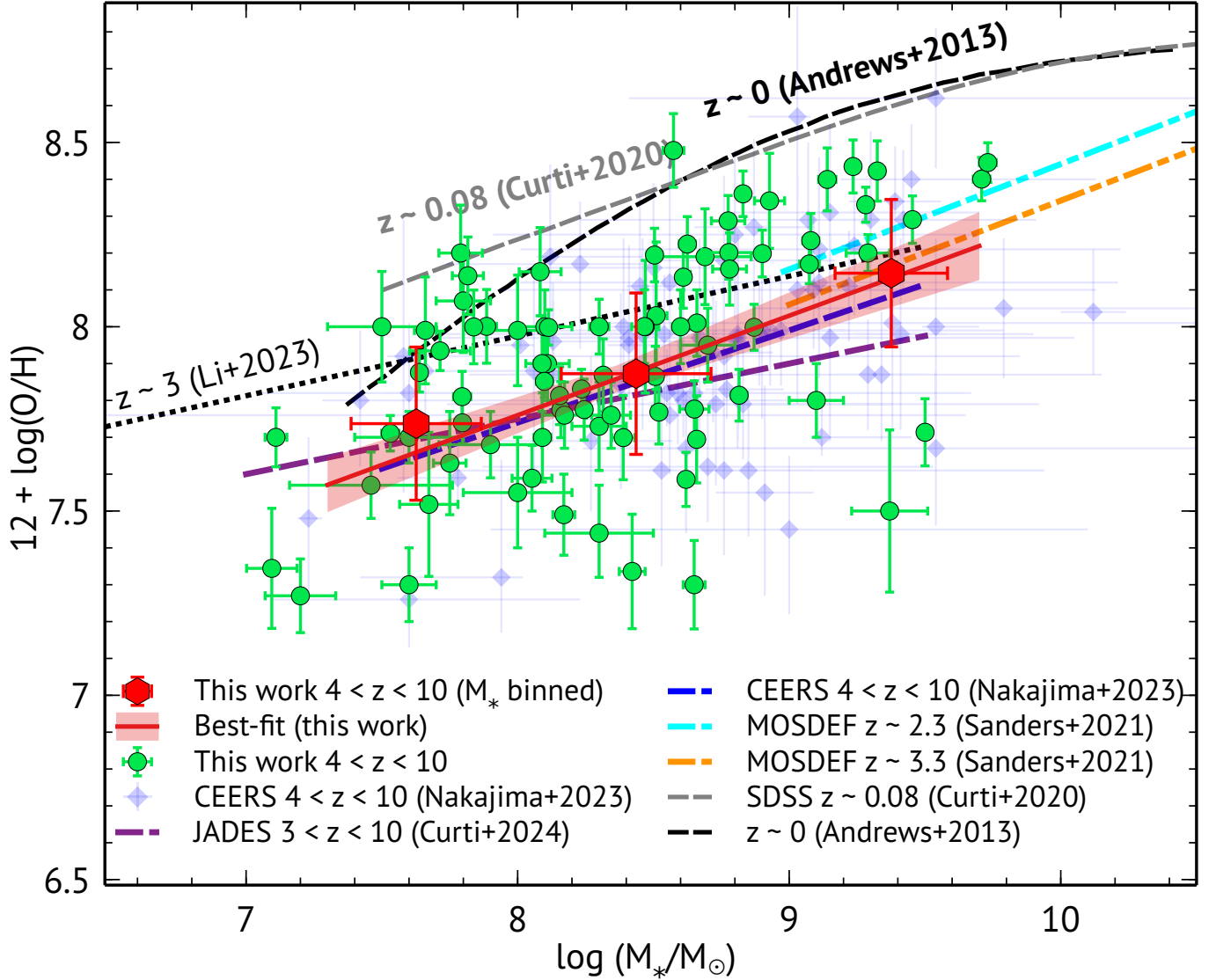


**Figure 4.** Stellar mass–gas-phase metallicity relation for our full sample with  $4 < z < 10$ . The green circles represent individual galaxies analyzed in this study. The green data points represent individual galaxies analyzed in this study. The sample is divided into three stellar mass ranges:  $M_* = 10^7 - 10^8$ ,  $10^8 - 10^9$ , and  $10^9 - 10^{10} M_\odot$ , with the average points shown as large red circles. The best-fit regression line for our complete sample, accompanied by its  $1\sigma$  uncertainty, is illustrated by the red line and the shaded region around it. We overplot our results with prior high-redshift and lower-redshift MZR measurements. Specifically, at high redshift, we reference the NIRSpec/CEERS survey for  $4 < z < 10$  galaxies shown with purple inverted squares (Nakajima et al. 2023), the NIRSpec/JADES survey for  $3 < z < 10$  galaxies (Curti et al. 2024) shown with purple dashed line. At lower redshifts, we compare with the MZR estimated by Andrews & Martini (2013) at  $z \sim 0$  (black dashed line) and Curti et al. (2020) at  $z \sim 0.08$  (gray dashed line), both using star-forming galaxies from the SDSS. Additionally, we reference Sanders et al. (2021), who estimated the MZR from the MOSDEF survey at  $z \sim 2.3$  (blue dashed line) and  $z \sim 3.3$  (orange dashed line), as well as Li et al. (2023), who estimated the MZR for dwarf galaxies at  $z \sim 3$  (black dotted line).

(Nakajima et al. 2023) and also with low-redshift galaxies at  $z = 0-3.3$  by Sanders et al. (2021) and He et al. (2024), however slightly higher than previous JADES studies (Curti et al. 2024).

Figure 4 clearly demonstrates that the metallicity at a given stellar mass in our sample is noticeably lower compared to the reference curve for  $z \sim 0$  from Andrews & Martini (2013) and for  $z \sim 0.08$  from Curti et al.

(2020). This difference is dependent on stellar mass, showing a variation of  $\sim 0.4$  dex at  $10^8 M_\odot$  and  $\sim 0.5$  dex at  $10^9 M_\odot$ . Compared to the MZR reported by Li et al. (2023) for galaxies at  $z \sim 2-3$ , our higher redshift sample exhibits a less prominent reduction in metallicity than the case of  $z \sim 0$ . The extent of this reduction is also mass-dependent, varying from  $\sim 0.2$  dex at  $10^8 M_\odot$  to  $\sim 0.08$  dex at  $10^9 M_\odot$ . A comparison with the MZR

from Sanders et al. (2021) at  $z \sim 2.3$  and  $z \sim 3.3$  reveals that the metallicity of our sample is marginally lower, by  $\sim 0.12$  dex at  $z \sim 2.3$  and  $\sim 0.03$  dex at  $z \sim 3.3$ , for a stellar masses of  $10^9 M_\odot$ .

We also compare our results with the previous studies that have examined the mass-metallicity relation at redshifts up to  $z \sim 10$ . Nakajima et al. (2023) performed an in-depth analysis of 135 galaxies using JWST/NIRSpec data from the ERO, GLASS, and CEERS programs, thereby illustrating the evolution of the mass-metallicity relations over the redshift range  $z = 4 - 10$ . Curti et al. (2024) utilized JWST/NIRSpec observations from the JADES deep GOODS-S tier to conduct a comprehensive analysis of the gas-phase metallicity properties in a sample of 66 low-stellar-mass galaxies ( $\log M_*/M_\odot \lesssim 9$ ) within the redshift range  $3 < z < 10$ . Despite minor variations in redshift intervals, our best-fit MZR for galaxies at  $z = 4 - 10$  closely aligns with the MZR observed by Nakajima et al. (2023), however steeper than that of Curti et al. (2024), as listed in Table 1. Nakajima et al. (2023) reported values of  $\gamma = 0.25 \pm 0.03$  and  $Z_{10} = 8.24 \pm 0.05$  for galaxies within  $4 < z < 10$ , while Curti et al. (2024) reported  $\gamma = 0.17 \pm 0.02$  and  $Z_{10} = 8.06 \pm 0.18$  for galaxies within  $3 < z < 10$ , derived from their  $\beta$  factor slope and gas-phase metallicity at a stellar mass of  $10^8 M_\odot$ .

To investigate the redshift evolution of MZR within the range of  $4 < z < 10$ , we divided our sample into three subsamples:  $z = 4-6$ ,  $6-8$ , and  $8-10$ . Our objective was to determine whether there is a noticeable change in the slope  $\gamma$  and normalization of the MZR across these redshift intervals. Table 1 compares the  $\gamma$  and  $Z_{10}$  values for these redshift bins, as well as for the complete sample spanning  $z = 4$  to  $10$ . Figure 5 presents the MZR for the three redshift intervals. Within these intervals, galaxies are binned by mass, with the average mass in each bin shown with red data points with error bars. We observe that the  $\gamma$  value for the  $z = 4$  to  $6$  interval is slightly higher ( $\gamma = 0.28 \pm 0.03$ ) compared to the  $z = 6$  to  $8$  ( $\gamma = 0.23 \pm 0.04$ ) and  $z = 8-10$  ( $\gamma = 0.21 \pm 0.04$ ), indicating a trend towards diminished metallicity and a flattening of the MZR slope as redshift increases. Such trend of decreasing metallicity in the highest-redshift bin is consistent with previous JWST studies by Nakajima et al. (2023) and Curti et al. (2024), who observed similar trends at higher redshifts. The evolution of MZR in our sample is also consistent with simulations, as further discussed in Section 7.

Given the limited size of our sample, conducting a statistically robust evaluation of the scatter in the scaling relationship remains challenging. However, we can get

an estimate of the intrinsic scatter using the equation:

$$\sigma_{\text{scatter}} = \sqrt{\sigma_{\text{obs}}^2 - \sigma_{\text{measured}}^2} \quad (8)$$

where  $\sigma_{\text{obs}}$  represents the observed scatter in the full sample around the best-fit MZR line, and  $\sigma_{\text{measured}}$  indicates the average uncertainty in the metallicity measurement.

We estimate  $\sigma_{\text{scatter}}$  to be approximately 0.16 dex for our entire sample of galaxies. This aligns with the intrinsic scatter of 0.16–0.18 dex found in dwarf galaxies at redshifts  $z = 2$  to  $3$  with stellar masses between  $10^8$  and  $10^9 M_\odot$  (Li et al. 2023); however larger than the intrinsic scatter of 0.08 dex observed in low-stellar-mass ( $\log M_*/M_\odot \lesssim 9$ ) galaxies at redshifts  $3 < z < 10$  (Curti et al. 2024).

## 6. THE FUNDAMENTAL METALLICITY RELATION

The scaling relations observed in galaxies are central to understanding galaxy formation and evolution. Among them, the SFR-MZ relation is particularly significant as it relates metallicity with stellar mass and SFR (e.g., Ellison et al. 2008; Mannucci et al. 2010; Lara-López et al. 2010; Andrews & Martini 2013; Hainline et al. 2020; Sanders et al. 2021; Li et al. 2023; Curti et al. 2024). Using a sample of 43,690 SDSS galaxies, Ellison et al. (2008) identified that galaxies with higher SFRs systematically show lower metallicities compared to their less star-forming counterparts of the same stellar mass. Expanding on this, Mannucci et al. (2010) and Lara-López et al. (2010) systematically demonstrated that incorporating SFR into the MZR significantly reduces its scatter. However, in a recent study using the MaNGA survey and TNG50 simulations, Ma et al. (2024) show that SFR alone does not significantly reduce scatter in the MZR. They further demonstrate that including galaxy size, along with SFR, significantly reduces this scatter.

Investigations of large galaxy samples from  $z = 3$  to  $0$  have shown minimal redshift evolution in the SFR-MZ relation for galaxies with masses above  $10^8 M_\odot$  (Henry et al. 2013b; Sanders et al. 2015; Curti et al. 2020; Henry et al. 2021). Au contraire, Pistis et al. (2024) found a modest yet statistically significant evolution in the MZR and FMR up to  $z \sim 0.63$ , highlighting the significance of stellar mass and SFR on gas-phase metallicity regardless of cosmic redshift. Multiple expressions describe the interdependencies of these three properties (Mannucci et al. 2010; Lara-López et al. 2010).

We utilize the method of Mannucci et al. (2010) to parameterize the SFR-MZ relation by determining the

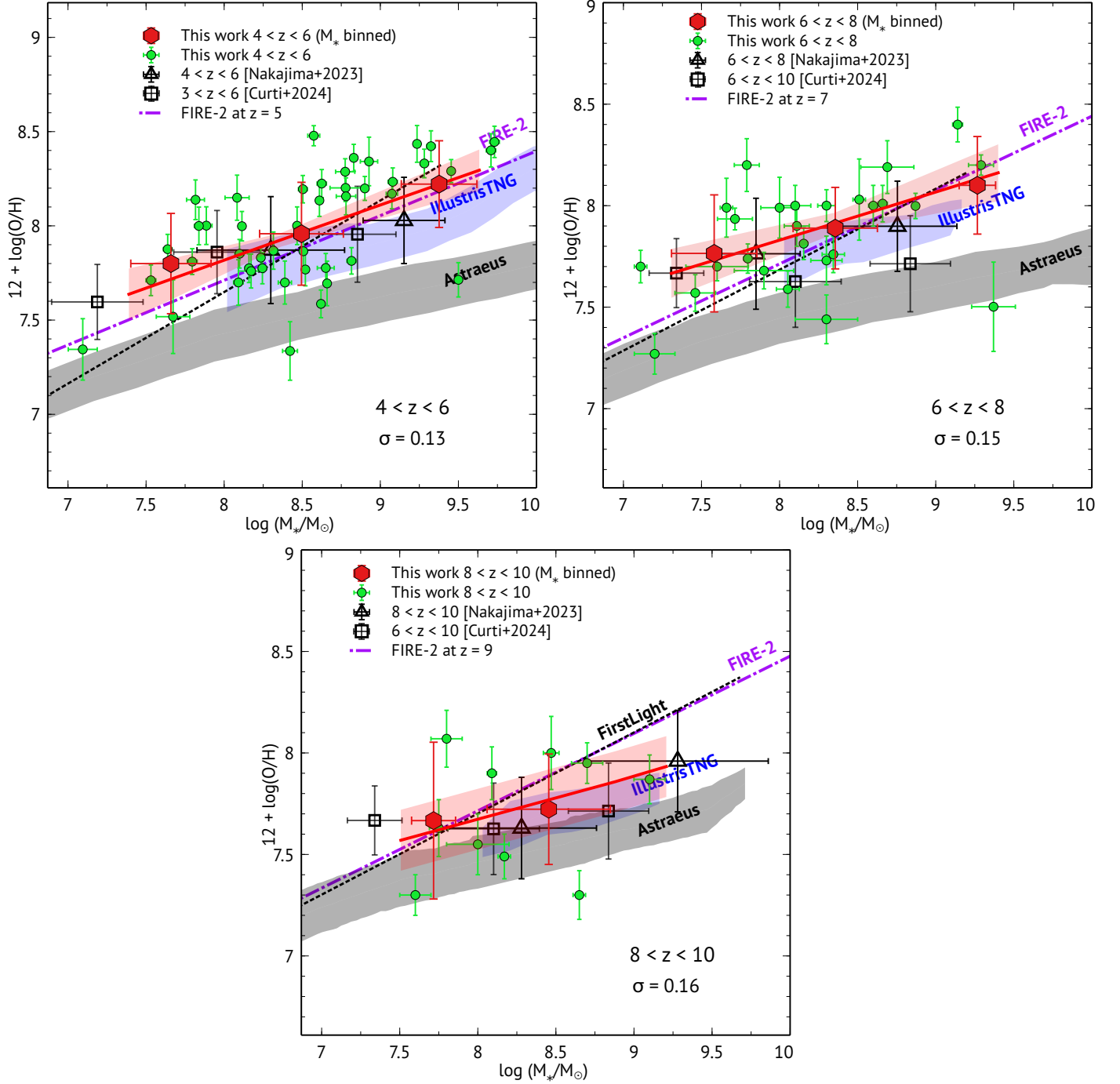


**Figure 5.** The mass-metallicity relation (MZR) is shown for three redshift intervals: 4–6, 6–8, and 8–10. For the  $z=4-6$  and  $z=6-8$  intervals, the sample is divided into three stellar mass ranges:  $M_* = 10^7 - 10^8$ ,  $10^8 - 10^9$ , and  $10^9 - 10^{10} M_\odot$ , with the averages depicted as large red circles. In the  $z = 8 - 10$  interval, due to the presence of only a single data point for  $M_* > 10^9 M_\odot$ , we compute averages for the  $M_* = 10^7 - 10^8$  and  $10^8 - 10^9$  ranges. The red circles indicate the mass-averaged values for each redshift interval, whereas the solid red lines represent the best-fit regression curves for each respective interval. The standard deviations of the residuals between the observations and the best-fit curves are represented by  $\sigma$ . See table 1 for the best-fit slopes and metallicity intercepts at each redshift intervals. We incorporate a comparative analysis of the MZR redshift evolution with findings from Nakajima et al. (2023), spanning the intervals 4 – 6, 6 – 8, and 8 – 10 (shown with open black triangles), as well as from Curti et al. (2024), covering the intervals 4 – 6 and 6 – 10 (shown with open black squares). The cosmological simulation outcomes for  $z = 5, 7$ , and  $9$  are also overlotted in the upper-left, upper-right, and bottom panels respectively. These include results from the FIRE-2 (dashed purple line, Marszewski et al. 2024), FirstLight (black dashed line, Langan et al. 2020), IllustrisTNG (blue shaded region, Torrey et al. 2019), and Astraerus (grey shaded region, Ucci et al. 2023) simulations. Extrapolated IllustrisTNG simulation in  $8 < z < 10$  are taken from Nakajima et al. (2023).

value of  $\alpha$  that minimizes the scatter in the oxygen-to-hydrogen ratio (O/H) at a fixed  $\mu_\alpha$ , defined as:

$$\mu_\alpha = \log\left(\frac{M_*}{M_\odot}\right) - \alpha \log\left(\frac{\text{SFR}}{M_\odot \text{ yr}^{-1}}\right). \quad (9)$$

Andrews & Martini (2013) showed that  $\alpha = 0.66$  minimizes the scatter of the local low-metallicity galaxies with a direct  $T_e$ -based metallicity in the  $\mu_\alpha$ -metallicity plane, resulting in

$$12 + \log(\text{O}/\text{H}) = 0.43 \times \mu_{0.66} + 4.58. \quad (10)$$

Andrews & Martini (2013) measurements extends down to  $\log(M_*/M_\odot) \sim 7.4$ . This is advantageous for comparing results with our sample since our sample has lower mass cutoff of around  $\sim 7.1 \pm 0.1$ . Figure 6 shows the SFR-MZ relation of galaxies our full sample on the  $\mu_\alpha$ -metallicity plane. The green data points represent our full sample, while the red hexagon data points indicate the weighted average in the stellar mass ranges:  $M_* = 10^7 - 10^8$ ,  $10^8 - 10^9$ , and  $10^9 - 10^{10} M_\odot$ . We also show that the  $z \sim 0$  relation by Andrews & Martini (2013), as defined in Equation 10. Our results are compared with the MOSDEF study at  $z \sim 2.3$  and  $z \sim 3.3$ , as detailed in Sanders et al. (2021). Additionally, we compare our findings with two recent JWST studies at similar redshift ranges, such as CEERS ( $4 < z < 10$ ; Nakajima et al. 2023) and JADES+CEERS ( $3 < z < 10$ ; Curti et al. 2024). We find that the average SFR-MZ relation of our sample of galaxies overlaps with those of previous JWST studies, the SFR-MZ relation at  $z \sim 0$  by Andrews & Martini (2013), and the relation derived from MOSDEF galaxies at  $z \sim 2.3$  and  $z \sim 3.3$  (Sanders et al. 2021).

Two other forms of the SFR-MZ relation have been derived by Curti et al. (2020) and Sanders et al. (2021) at  $z \sim 0$ . Specifically, Curti et al. (2020) and Sanders et al. (2021) identified  $\alpha = 0.55$  and  $\alpha = 0.6$ , respectively, as yielding the most precise 2D projection of the fundamental metallicity relation on the O/H versus  $\mu_\alpha$  plane, with minimal scatter, derived from composite SDSS spectra. We utilize the SFR-MZ relation from Andrews & Martini (2013) with  $\alpha = 0.66$  due to its alignment with the parameter space examined in this study. Specifically, the metallicity measurements in Andrews & Martini (2013) span three decades in stellar mass, from  $\log(M_*/M_\odot) \simeq 7.4$  to 10.5, with 78 out of 81 galaxies in our sample falling within this range. In contrast, Curti et al. (2020) and Sanders et al. (2021) span the higher stellar mass range, from  $\log(M_*/M_\odot) \simeq 8.5$  to 11.4, which is outside the range of the majority of our galaxy stellar masses.

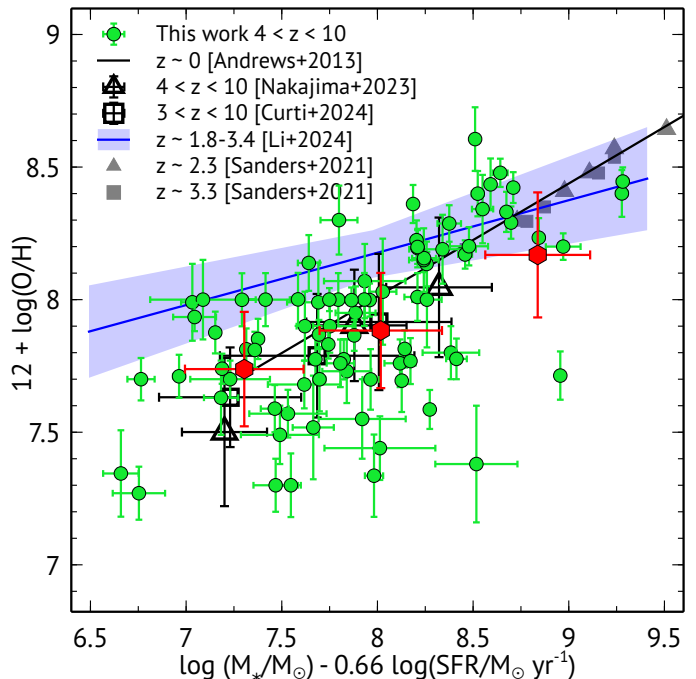


**Figure 6.** Projection of the SFR-MZ relation in O/H versus  $\mu_{0.66} = \log(M_*/M_\odot) - 0.66 \times \log(\text{SFR}/M_\odot \text{ yr}^{-1})$  plane, where  $\alpha = 0.66$  minimizes the scatter of the local low-metallicity galaxies. The green data points represent our entire sample, while the red hexagons indicate the weighted averages within the stellar mass ranges of  $M_* = 10^7 - 10^8$ ,  $10^8 - 10^9$ , and  $10^9 - 10^{10} M_\odot$ . The solid black line represents the SFR-MZ relation at  $z \sim 0$  from Andrews & Martini (2013), while the grey filled triangles and squares indicate the  $z \sim 2.3$  and  $z \sim 3.3$  SFR-MZ relations from Sanders et al. (2021). The solid blue line depicts the SFR-MZ relation for dwarf galaxies at  $z \sim 2 - 3$  from Li et al. (2023), with the blue shaded region showing its  $1\sigma$  uncertainty.

We next investigate that if there are any redshift evolution of the SFR-MZ relations that we adopted above. Figure 7 shows the metallicity residuals at fixed  $\mu_{0.66}$  of our  $4 < z < 10$  sample compared to the SFR-MZ relation of Andrews & Martini (2013) at  $z \sim 0$ . The metallicity residual is calculated as follows:

$$\Delta \log(\text{O}/\text{H}) = (12 + \log(\text{O}/\text{H}))_{\text{obs}} - (12 + \log(\text{O}/\text{H}))_{\alpha=0.66}. \quad (11)$$

The green circles represent the full sample of  $4 < z < 10$ . We also divided the  $z = 4 - 10$  sample into three redshift bins:  $z = 4 - 6$ ,  $z = 6 - 8$ , and  $z = 8 - 10$ , and calculated their weighted-mean offset from the local Andrews & Martini (2013) SFR-MZ relation, which are shown with red hexagons. We find the weighted-mean offset for the  $z = 4 - 6$  bin to be  $\Delta \log(\text{O}/\text{H}) \sim -0.01$  dex, while for the  $z = 6 - 8$  bin, it is  $\Delta \log(\text{O}/\text{H}) \sim -0.02$  dex. This consistency suggests that a unified relation between SFR and MZ accurately characterizes the av-

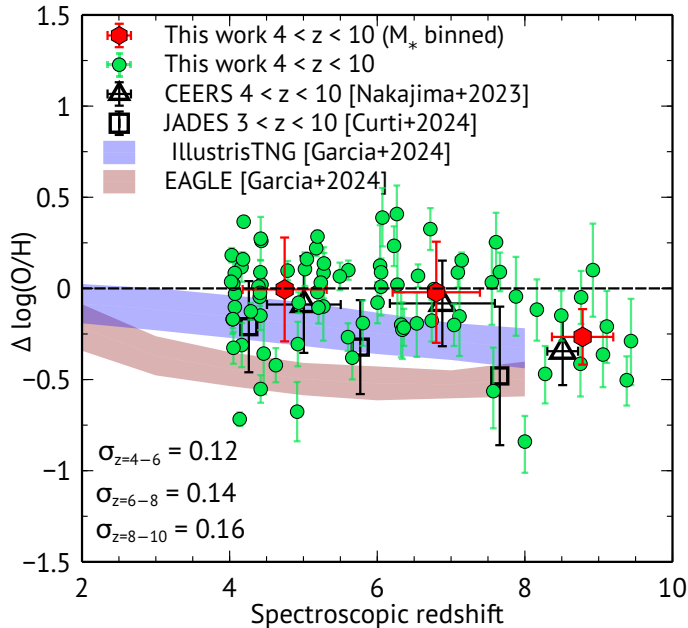


**Figure 7.** The discrepancies in metallicity between our sample galaxies and the predictions of the local Fundamental Metallicity Relation (FMR) by Andrews & Martini (2013) as a function of redshift. The green data points represent our full sample, while the red data points indicate the weighted average of the discrepancies in three redshift bins:  $z = 4 - 6$ ,  $z = 6 - 8$ , and  $z = 8 - 10$ . The standard deviations of the residuals in each redshift bin are denoted by  $\sigma$ . Redshift-binned deviations from the local FMR, taken from Nakajima et al. (2023) for three bins of redshift  $z = 4 - 6$ ,  $z = 6 - 8$ , and  $z = 8 - 10$ , and from Curti et al. (2024) for three bins of redshift  $z = 3 - 5$ ,  $z = 5 - 7$ , and  $z = 7 - 10$ , are shown with open black triangles and open black squares, respectively. This plot demonstrates that metallicity remains relatively constant up to  $z \sim 8$ , but there is a marked decline in metallicity beyond  $z > 8$ . We also compared our results with IllustrisTNG (blue shade) and EAGLE (dark red shade) cosmological simulations.

erage properties of galaxy samples from  $z = 0$  to  $z \sim 8$ , indicating weak/no significant redshift evolution of the SFR-MZ relations up to  $z \sim 8$ . However, a significant decrease in metallicity is observed beyond  $z > 8$  surpassing the error margins, with  $\Delta \log(\text{O}/\text{H}) \sim -0.27$  dex.

A similar conclusion has been reached by Nakajima et al. (2023) for their CEERS galaxy sample within the redshift range  $4 < z < 10$ . They found no deviation from the SFR-MZ relation of Andrews & Martini (2013) for both the  $z = 4 - 6$  and  $z = 6 - 8$  intervals, but for the  $z = 8 - 10$  interval, they reported  $\Delta \log(\text{O}/\text{H}) \sim -0.3$  dex, showing a significant decrease in metallicity beyond  $z > 8$ . These findings also align with Heintz

et al. (2023), who compared their  $z > 7$  galaxy sample from the Abell 2744, RXJ-2129, and CEERS fields, and with the observations by Matthee et al. (2023) of strong [O III]-emitting galaxies at  $z = 5 - 7$ , showing no significant evolution in metallicity from  $z \approx 6$  to  $z \approx 8$ . In contrast, the JADES+CEERS sample study by Curti et al. (2023) investigated low-mass ( $\log(M_*/M_\odot) \lesssim 8.5$ ) galaxies at  $3 < z < 10$  and found a tentative decrease in metallicity and a deviation from the local SFR-MZ relation of Curti et al. (2020) beyond  $z > 6$ . However, the redshift where the SFR-MZ relation starts to deviate from the local SFR-MZ relation, such as at  $z \approx 6$  or  $z \approx 8$ , can arise from the use of different local SFR-MZ relations with varying values of  $\alpha$ . In fact, Nakajima et al. (2023) found that using the formalism of Curti et al. (2020) for the local SFR-MZ relation, instead of the Andrews & Martini (2013) SFR-MZ relation for the local universe, leads to a metallicity deviation in the SFR-MZ relation at  $z \sim 6$ . However, we adhere to the Andrews & Martini (2013) SFR-MZ relation at  $z \sim 0$  because the mass range of our sample is most consistent with the mass range of their formalism.

We have also compared our results with the IllustrisTNG (Springel et al. 2018; Nelson et al. 2019a,b) and EAGLE (McAlpine et al. 2016) simulations, as depicted in Figure 7. In both simulations, there is an observed negative shift from zero that increases with redshift. Specifically, in TNG, the deviations from the  $z = 0$  calibrated FMR linearly become more negative as redshift increases. In EAGLE, these deviations continue to become more negative up to  $z \sim 5$  and then stabilize from  $z = 6$  to  $z = 8$  (for more details, see Garcia et al. 2024a). The negative offsets observed in our galaxy sample are consistent with those in the IllustrisTNG simulation for  $z < 8$ , similar to findings by Nakajima et al. (2023). However, it is important to note that these conclusions strongly depend on the chosen local FMR relation and the sample size of high-redshift galaxies, both in simulations and observations.

## 7. IS METALLICITY REDSHIFT INVARIANT?

Gas-phase metallicity is a crucial indicator of the current evolutionary state of galaxies. Prior to JWST, the MZR and its evolution were widely studied within redshift  $z \lesssim 3$  (e.g., Erb et al. 2006a; Zahid et al. 2012, 2013; Henry et al. 2013a,b; Maier et al. 2014; Steidel et al. 2014; Sanders et al. 2015). Specifically, Zahid et al. (2013) demonstrated that for a given stellar mass, gas-phase metallicity is inversely proportional to redshift in the range  $0 < z < 2.3$ . With smaller galaxy samples Maiolino et al. (2008b) and Mannucci et al. (2009) also confirmed the existence of the MZR up to  $z = 3$ .

Several simulations have also explored the MZR and its evolution at high redshifts, such as FIRE-1 (Ma et al. 2016), IllustrisTNG (Vogelsberger et al. 2014b; Torrey et al. 2019; Garcia et al. 2024b,a), FirstLight (Langan et al. 2020), SERRA (Pallottini et al. 2022), ASTRAEUS (Ucci et al. 2023), FLARES (Wilkins et al. 2023), and FIRE-2 (Marszewski et al. 2024). FIRE-1 simulations covered redshifts from  $z = 0$  to 6. Recently, FIRE-2 simulations extended this study to the redshift range  $z = 5$  to 12 showing that the normalization of the MZR evolves weakly for  $z \geq 3$ . Torrey et al. (2019) investigated the distribution and evolution of metals within the IllustrisTNG simulation suite, focusing on the gas-phase MZR and its redshift evolution over a stellar-mass range of  $10^8 < M_*/M_\odot < 10^{10.5}$  and redshift range of  $0 < z < 10$ . IllustrisTNG galaxies broadly reproduce the MZR slope and normalization out to  $z = 2$ . Interestingly, they found a declining trend of gas-phase metallicity with redshift, with metallicity at  $z = 8$  being 0.5 dex lower than at  $z=0$ .

We compare the MZR for our full sample of 81 galaxies with numerous simulations and further compared redshift evolution of gas-phase metallicity with FIRE-2 and IllustrisTNG simulations, as shown in Figure 5 and 8.

Figure 5 shows the comparison of the MZR with simulations across three redshift bins:  $z = 4-6$ ,  $6-8$ , and  $8-10$ . As discussed in Section 5, our mass-averaged metallicities align with two previous JWST observations by Curti et al. (2024) and Nakajima et al. (2023). We found that within  $z < 6$ , our best-fit MZR normalization and slope are consistent with FIRE-2 and IllustrisTNG, but significantly higher than the Astraeus simulation. For the redshift bins  $z = 6-8$  and  $8-10$ , our best-fit MZR slope is flatter compared to FIRE-2 and FirstLight but matches well with IllustrisTNG. Our best-fit MZR normalizations are  $\sim 0.14$  dex and 0.36 dex lower than those of FIRE-2 and FirstLight in the same redshift bins, but they are consistent with the extrapolated IllustrisTNG simulation.

As discussed in Section 6, the investigation of redshift evolution through the SFR-MZR relation is highly dependent on the models used. This approach yields significantly varied results across different models. Garcia et al. (2024b) showed that the slope of the anti-correlation of offset from the MZR with SFR changes with redshift. We, therefore, conducted a more detailed analysis of the evolution of metallicities across redshifts ranging from 4 to 10. In this analysis, we integrated our dataset of 81 galaxies with data from two recent JWST studies by Nakajima et al. (2023) and Curti et al. (2024), which both encompass similar ranges in redshift and stellar mass ( $10^7 \lesssim M_*/M_\odot \lesssim 10^{10}$ ). Although

the study by Curti et al. (2024) includes galaxies from a slightly broader redshift range of 3 to 10, for consistency in our analysis, we only considered galaxies with redshifts  $z \geq 4$ . This approach resulted in an extensive sample of 263 star-forming galaxies. We depicted the metallicities of these galaxies on a  $12+\log(\text{O}/\text{H})-z$  plane, as shown in Figure 8. We further calculated the average metallicities for the entire sample (263 galaxies) across each redshift interval of  $\Delta z = 1$  (between  $z = 4$  to 10), as shown in red hexagons in Figure 8. Additionally, we included iso-stellar mass curves from the IllustrisTNG, EAGLE, and FIRE-2 simulations for stellar masses of  $\log(M_*/M_\odot) = 8$  and 10.

Our findings indicate a discernible decrease in metallicity as the redshift increases, a trend that aligns with results from Roberts-Borsani et al. (2024), who observed similar declines in their study of stacked metallicities for galaxies between redshifts of 5.5 and 9.5. To quantitatively compare our results with these simulations, we fit a linear regression to our full sample. The best-fit line, depicted in Figure 8, showed a slope of  $0.067 \pm 0.013$  and an intercept of  $8.31 \pm 0.10$ . This slope is more consistent with predictions from the IllustrisTNG than those from FIRE-2 and EAGLE, bolstering the observation of a steady decrease in metallicity with increasing redshift. These results corroborate our earlier findings, which suggested lower mass-averaged MZR at  $z > 8$ . While a detailed comparison between IllustrisTNG and FIRE-2 is beyond the scope of this paper, the key difference lies in their ISM treatment: TNG uses sub-grid prescriptions, resulting in smooth star formation and feedback, while FIRE models these processes locally and explicitly, leading to rapid, bursty star formation and feedback (e.g., Sparre et al. 2017). This bursty behavior is thought to regulate early galaxy growth and may convert dark matter cusps into cores, making it critical for understanding both galaxy formation and dark matter (Hayward & Hopkins 2017; Faucher-Giguère 2018). JWST observations of high-redshift galaxies show a continued metallicity decrease, which aligns more with TNG’s smooth feedback model than FIRE’s bursty predictions.

We also examine whether the redshift evolution of metallicity observed in our analysis is driven by the intrinsic evolution of stellar mass within our sample. The bottom panel of Figure 8 presents stellar mass as a function of redshift for the 263 galaxies. The stellar masses are well distributed around a median value of 8.35 within the redshift range  $4 < z < 10$ , indicating no significant evolution in stellar mass. This confirms that the redshift evolution of metallicity observed in this work has a physical origin, warranting further investigation.

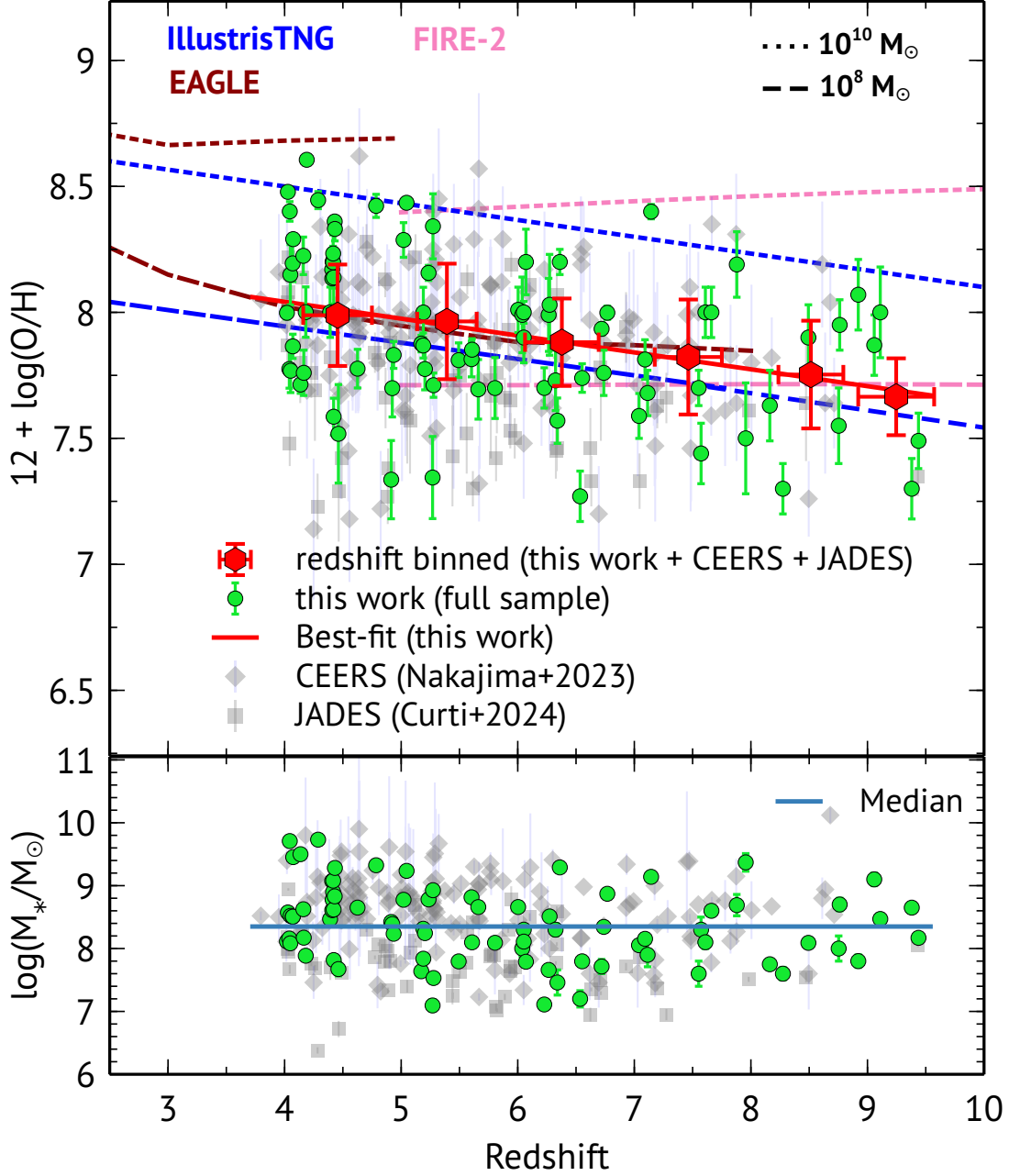


**Figure 8.** Top: Comparing redshift evolution of gas-phase metallicity of our full sample + galaxies from earlier CEERS and JADES studies with IllustrisTNG (Torrey et al. 2019), FIRE-2 (Marszewski et al. 2024), and EAGLE (Garcia et al. 2024a) simulations. Red data points present the redshift-averaged metallicity in  $z = 4\text{--}10$  with  $\Delta z=1$  size bin for full 263 galaxies (this work + CEERS + JADES). Red solid line shows the best-fit line for redshift averaged metallicity. The sample from earlier CEERS (Nakajima et al. 2023) and JADES (Curti et al. 2024) studies are shown in grey diamond and squares, respectively. The iso-stellar mass curves at  $M_* = 10^8 M_\odot$  (dashed) and  $10^{10} M_\odot$  (dotted) predicted by simulations are shown in blue (IllustrisTNG), pink (FIRE-2), and darkred (EAGLE) lines. Bottom: Stellar mass vs redshift for the full sample. The light-blue line shows the median stellar mass. The data points are well distributed around this median line, suggesting no significant evolution in stellar masses.

We explore an empirical relationship among gas-phase metallicity, stellar mass, and redshift. Figure 9 presents a 3D representation of the metallicities of 263 galaxies, shown as functions of both stellar mass and redshift. We introduce an empirical relation with the following functional form:

$$12 + \log(\text{O}/\text{H}) = Z_0 + \alpha \log\left(\frac{M_*}{M_\odot}\right) - \beta(1 + z), \quad (12)$$

We find the best-fit values for our full sample to be,  $Z_0 = 6.29 \pm 0.22$ ,  $\alpha = 0.237 \pm 0.023$ , and  $\beta = 0.06 \pm 0.01$ . The corresponding best-fit surface and the posterior distribution of the fitting parameters are shown in Figure 9. It is important to note that while our sample spans a stellar mass range from  $10^7 < M_*/M_\odot < 10^{10}$  and a redshift range from  $4 < z < 10$ , this simple empirical model does not account for any potential flattening in metallicity, as previously shown in Curti et al. (2020) and Sanders et al. (2021). Our best-fit model effectively captures the observed trends, demonstrating an increase in metallicity with stellar mass and a decrease with rising redshift, providing a well represented MZ–redshift relation. We also note that current JWST observations predominantly target massive, high-redshift galaxies ( $z > 8$ ), which generally exhibit higher metallicity compared to lower-mass, metal-poor galaxies. This selection bias may influence the observed slope for redshift evolution, potentially over-estimating it. We anticipate that the inclusion of high- $z$ , low-mass galaxies in future JWST observations could reveal a steeper slope for this evolutionary trend.

The primary factors driving the evolution of gas-phase metallicity is currently a “Grand Challenge” problem in cosmology. Galactic metallicity evolutionary trends with redshift or mass have been explained by competing scenarios, such as changes in metal retention efficiency or changes in the gas fractions of galaxies (e.g., Ma et al. 2016; Torrey et al. 2019; Langan et al. 2020; Bassini et al. 2024). A relatively high efficiency of metal ejection via AGN/stellar feedback processes has been found in high-mass galaxies, which in turn reduces the retained metal budget of these galaxies (Suresh et al. 2015). Torrey et al. (2019) found that metal retention efficiency increases with redshift in IllustrisTNG galaxies, which directly contradicts the observed decline in metallicity with increasing redshift. However, they also found that the gas fraction, defined as the ratio between ISM gas mass and stellar mass, increases with redshift in high-redshift galaxies, serving as a significant contributing factor to the observed MZR evolution. Increased gas fractions due to gas inflow dilute the metal-enriched gas in the ISM, effectively decreasing the metallicity. The

MZR for our sample of galaxies shows a similar declining trend as seen in IllustrisTNG, suggesting that increased gas fractions (e.g., galactic inflows) may drive the low MZR normalization in high-redshift galaxies. We need more theoretical studies and baseline models to understand the physics behind the decreasing metallicity trend towards early universe.

## 8. SUMMARY

In this study, we investigated the evolution of the mass-metallicity relation (MZR) and the fundamental metallicity relation (FMR) using a sample of 81 galaxies observed by JWST/NIRSpec spanning a stellar mass range of  $10^7 < M_*/M_\odot < 10^{10}$  and a redshift range of  $4 < z < 10$ . The sample comprises galaxies from the JADES GOODS-N and GOODS-S fields, the JWST-PRIMAL Legacy Survey, and additional galaxies from the literature in the Abell 2744, SMACS-0723, RXJ2129, BDF, COSMOS, and MACS1149 fields, which were previously not utilized for these scaling relations.

Our main findings are summarized below:

- For metallicity determination, our analysis focused on the emission lines observed with the medium-resolution grating: [O III] $\lambda$ 5007, [O II] $\lambda$ 3727, 29, H $\beta$ , H $\alpha$ , [N II] $\lambda$ 6584, and [S II] $\lambda$ 6716,31. Prior to conducting the metallicity analysis, we corrected for dust reddening by estimating the Balmer decrement using the H $\alpha$ /H $\beta$  and H $\gamma$ /H $\beta$  ratios, employing the reddening curve from Calzetti et al. (2000). We then utilized the reddening-corrected line ratios R3 and O32/N2/S2, along with the calibrations developed by Curti et al. (2020), to determine metallicities through line ratio diagnostics. For the primary metallicity calibration, we employed R3 indices. To address potential degeneracy inherent in these calibrations, we further utilized the O32/N2/S2 line ratios to refine and accurately determine the metallicities. To ensure precise metallicity measurements, we excluded sources with potential AGN emission, as AGN-driven ionization disrupts the standard calibrations for star-forming galaxies, by employing the Mass-Excitation diagnostic diagrams introduced by Juneau et al. (2014) and refined by Coil et al. (2015).
- We estimated SFRs from the reddening-corrected H $\beta$  luminosity using calibrations provided by Figueira et al. (2022) for star-forming galaxies identified through the Mass-Excitation (MEX) diagnostic diagram. We examine the relationship between stellar mass and star formation rate for

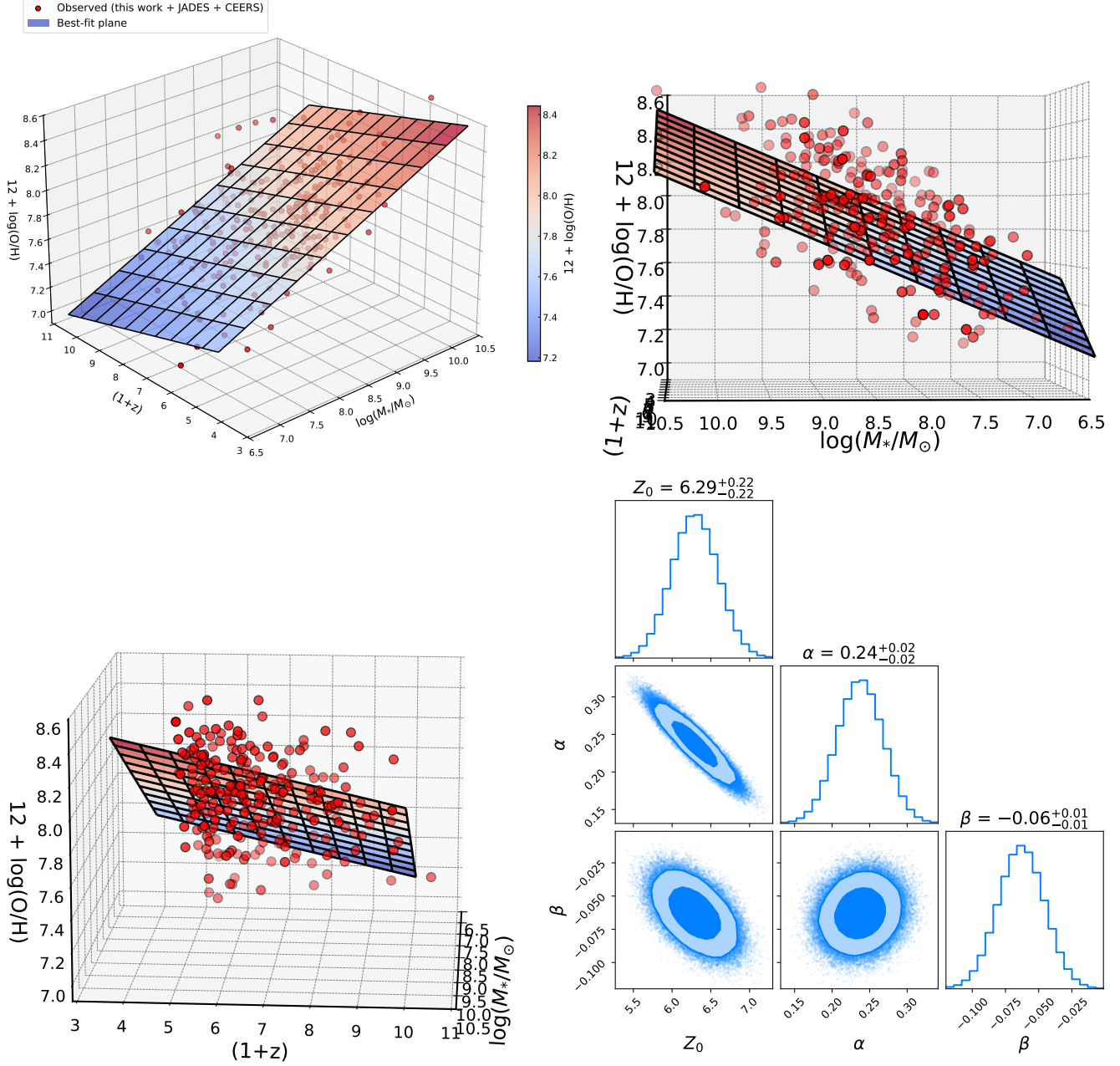


**Figure 9.** Top-right to bottom-left anticlockwise: 3D visualization the mass–metallicity–redshift (MZ– $z$ ) relation for our full sample of 263 galaxies, including 81 galaxies from this work, 135 galaxies from CEERS (Nakajima et al. 2023), 47 galaxies from JADES (Curti et al. 2024). The surface representing the best-fitting MZ– $z$  relation is displayed, and the histogram of metallicity dispersion for individual galaxies relative to this surface is illustrated in the colorbar. Bottom-right: posterior distribution of the best-fit parameters,  $Z_0$ ,  $\alpha$ , and  $\beta$  of the mass–metallicity–redshift (MZ– $z$ ) relation.

our full sample, which demonstrates a positive correlation throughout the redshift range of  $z \sim 4 - 10$ , consistent with previous observations and main sequence galaxies.

- We examined the stellar mass–metallicity relation (MZR) for high-redshift galaxies using 81 galaxies spanning a redshift range of  $z = 4 - 10$  and the stellar mass range of  $M_* = 10^7 - 10^{10} M_\odot$ .

We found the best-fit  $Z_{10} = 8.28 \pm 0.08$  and  $\gamma = 0.27 \pm 0.02$  for our full sample. When comparing our MZR with those of lower redshift galaxies, we found weak evolution in the MZ relation. Compared to the MZR documented by Li et al. (2023) for galaxies at  $z \sim 2 - 3$ , our  $4 < z < 10$  sample shows a small reduction in metallicity, ranging within  $\Delta \log(\text{O}/\text{H}) \sim 0.2$  at  $10^8 M_\odot$  and

$\Delta \log(\text{O}/\text{H}) \sim 0.07$  at  $10^9 M_\odot$ . In comparison to the MZR at  $z \sim 3.3$  from Sanders et al. (2021) extrapolated to the lower-mass regime, our sample shows a slight average reduction in  $\log(\text{O}/\text{H})$ , with a  $\Delta \log(\text{O}/\text{H})$  of 0.03 dex. We also compared our MZR with recent JWST studies of high-redshift galaxies. Despite variations in redshift and mass intervals, our best-fit MZR for galaxies at  $z = 4 - 10$  closely aligns with earlier studies by Nakajima et al. (2023), Heintz et al. (2023), Shapley et al. (2023), and Curti et al. (2024), with their MZR slopes/predictions consistent with our findings.

- To investigate the redshift evolution of the MZR from  $z = 4$  to  $z = 10$ , we segmented our sample into three distinct groups:  $z = 4$  to 6,  $z = 6$  to 8, and  $z = 8$  to 10. We find a steeper MZR slope ( $\gamma = 0.28 \pm 0.03$ ) for the  $z = 4$  to 6 compared to the  $z = 6$  to 8 ( $\gamma = 0.23 \pm 0.04$ ) and the  $z = 8$  to 10 ( $\gamma = 0.21 \pm 0.04$ ). This observation suggests a gentle decline in metallicity. The observed trend of decreasing metallicity at higher redshifts is consistent with the findings of Nakajima et al. (2023) and Curti et al. (2024), who reported similar trends in their studies.
- We investigated the SFR-MZ relation, also known as the Fundamental Metallicity Relation (FMR), for our entire sample using the parameterization from Andrews & Martini (2013), with  $\alpha = 0.66$  in  $\mu_\alpha$ . Within redshift range  $z \sim 4-8$ , we observed no evolution in SFR-MZ relation, suggesting that galaxies maintain metallicity equilibrium through star formation, the inflow of pristine gas, and the outflow of metal-enriched gas. However, we found a significant decrease in metallicity ( $\Delta \log(\text{O}/\text{H}) = 0.27$  dex) at  $z > 8$ , consistent with previous JWST observations by Nakajima et al. (2023). This suggests that early-stage galaxies may not yet have reached a state of metallicity equilibrium, likely due to their nascent stage of formation.
- We further explored the redshift evolution of metallicity within the range  $4 < z < 10$  by integrating samples from two major JWST studies into our analysis. This includes 135 galaxies from CEERS (Nakajima et al. 2023) and 47

galaxies from JADES (Curti et al. 2024). Our analysis revealed a distinct decreasing trend in redshift-averaged metallicities, with a slope of  $0.067 \pm 0.013$ . This trend aligns with predictions from the IllustrisTNG simulations (Torrey et al. 2019) and corroborates previous JWST observations in the redshift range  $5.5 < z < 9.5$  (Roberts-Borsani et al. 2024).

- We also introduce an empirical mass-metallicity-redshift (MZ- $z$ ) relation that captures the observed trends, including increasing metallicity with rising stellar mass and decreasing metallicity with increasing redshift. We find the best-fit MZ- $z$  for our full sample of galaxies:  $12 + \log(\text{O}/\text{H}) = (6.29 \pm 0.10) + (0.237 \pm 0.023) \times \log\left(\frac{M_*}{M_\odot}\right) - (0.06 \pm 0.01) \times (1 + z)$ . The observed decline in metallicity at higher redshifts points to complex, possibly unexplored, physical processes that modulate star formation, gas inflow, and outflow, thereby impacting the ISM metal content in galaxies.

1 We sincerely thank the anonymous referee for their in-  
 2 sightful comments and suggestions. A.S acknowledges  
 3 support from NASA via sub-award SV2-82023 from  
 4 the Chandra X-ray Center and via sub-award S001534-  
 5 NASA from the Pennsylvania State University. The au-  
 6 thors also acknowledge the MIT SuperCloud and Lin-  
 7 coln Laboratory Supercomputing Center for providing  
 8 (HPC, database, consultation) resources that have con-  
 9 tributed to the research results reported within this pa-  
 10 per. PT and AMG acknowledge support from NSF-AST  
 11 2346977. This work is based on observations made with  
 12 the NASA/ESA/CSA James Webb Space Telescope.  
 13 The data were obtained from the Mikulski Archive for  
 14 Space Telescopes at the Space Telescope Science Insti-  
 15 tute, which is operated by the Association of Universi-  
 16 ties for Research in Astronomy, Inc., under NASA con-  
 17 tract NAS 5-03127 for JWST. JADES data products  
 18 presented herein were retrieved from the data release  
 19 3 archive <https://jades-survey.github.io/scientists/data.html>.  
 20 Primal Survey data products presented herein  
 21 were retrieved from the DAWN JWST Archive (DJA).  
 22 DJA is an initiative of the Cosmic Dawn Center, which  
 23 is funded by the Danish National Research Foundation  
 24 under grant DNRFF140.

## REFERENCES

Abazajian, K., Adelman-McCarthy, J. K., Agüeros, M. A.,  
 et al. 2003, AJ, 126, 2081, doi: [10.1086/378165](https://doi.org/10.1086/378165)

Anders, E., & Grevesse, N. 1989, GeoCoA, 53, 197,  
 doi: [10.1016/0016-7037\(89\)90286-X](https://doi.org/10.1016/0016-7037(89)90286-X)

- Andrews, B. H., & Martini, P. 2013, *ApJ*, 765, 140, doi: [10.1088/0004-637X/765/2/140](https://doi.org/10.1088/0004-637X/765/2/140)
- Baldwin, J. A., Phillips, M. M., & Terlevich, R. 1981, *PASP*, 93, 5, doi: [10.1086/130766](https://doi.org/10.1086/130766)
- Bassini, L., Feldmann, R., Gensior, J., et al. 2024, *MNRAS*, 532, L14, doi: [10.1093/mnrasl/slae036](https://doi.org/10.1093/mnrasl/slae036)
- Behroozi, P. S., Wechsler, R. H., & Conroy, C. 2013, *ApJ*, 770, 57, doi: [10.1088/0004-637X/770/1/57](https://doi.org/10.1088/0004-637X/770/1/57)
- Bezanson, R., Labbe, I., Whitaker, K. E., et al. 2022, arXiv e-prints, arXiv:2212.04026, doi: [10.48550/arXiv.2212.04026](https://doi.org/10.48550/arXiv.2212.04026)
- Bian, F., Kewley, L. J., & Dopita, M. A. 2018, *ApJ*, 859, 175, doi: [10.3847/1538-4357/aabd74](https://doi.org/10.3847/1538-4357/aabd74)
- Bruzual, G., & Charlot, S. 2003, *MNRAS*, 344, 1000, doi: [10.1046/j.1365-8711.2003.06897.x](https://doi.org/10.1046/j.1365-8711.2003.06897.x)
- Bunker, A. J., Cameron, A. J., Curtis-Lake, E., et al. 2023, arXiv e-prints, arXiv:2306.02467, doi: [10.48550/arXiv.2306.02467](https://doi.org/10.48550/arXiv.2306.02467)
- Calzetti, D., Armus, L., Bohlin, R. C., et al. 2000, *ApJ*, 533, 682, doi: [10.1086/308692](https://doi.org/10.1086/308692)
- Calzetti, D., Kinney, A. L., & Storchi-Bergmann, T. 1994, *ApJ*, 429, 582, doi: [10.1086/174346](https://doi.org/10.1086/174346)
- Carnall, A. C., McLure, R. J., Dunlop, J. S., & Davé, R. 2018, *MNRAS*, 480, 4379, doi: [10.1093/mnras/sty2169](https://doi.org/10.1093/mnras/sty2169)
- Chabrier, G. 2003, *PASP*, 115, 763, doi: [10.1086/376392](https://doi.org/10.1086/376392)
- Chakraborty, P., Sarkar, A., Wolk, S., et al. 2024, arXiv e-prints, arXiv:2406.05306, doi: [10.48550/arXiv.2406.05306](https://doi.org/10.48550/arXiv.2406.05306)
- Chatzikos, M., Bianchi, S., Camilloni, F., et al. 2023, *RMxAA*, 59, 327, doi: [10.22201/ia.01851101p.2023.59.02.12](https://doi.org/10.22201/ia.01851101p.2023.59.02.12)
- Coil, A. L., Aird, J., Reddy, N., et al. 2015, *ApJ*, 801, 35, doi: [10.1088/0004-637X/801/1/35](https://doi.org/10.1088/0004-637X/801/1/35)
- Cresci, G., & Maiolino, R. 2018, *Nature Astronomy*, 2, 179, doi: [10.1038/s41550-018-0404-5](https://doi.org/10.1038/s41550-018-0404-5)
- Cresci, G., Mannucci, F., & Curti, M. 2019, *A&A*, 627, A42, doi: [10.1051/0004-6361/201834637](https://doi.org/10.1051/0004-6361/201834637)
- Curti, M., Cresci, G., Mannucci, F., et al. 2017, *MNRAS*, 465, 1384, doi: [10.1093/mnras/stw2766](https://doi.org/10.1093/mnras/stw2766)
- Curti, M., Mannucci, F., Cresci, G., & Maiolino, R. 2020, *MNRAS*, 491, 944, doi: [10.1093/mnras/stz2910](https://doi.org/10.1093/mnras/stz2910)
- Curti, M., Maiolino, R., Curtis-Lake, E., et al. 2023, *JADES: Insights on the low-mass end of the mass-metallicity-star-formation rate relation at  $3 < z < 10$  from deep JWST/NIRSpec spectroscopy.* <https://arxiv.org/abs/2304.08516>
- Curti, M., Maiolino, R., Curtis-Lake, E., et al. 2024, *A&A*, 684, A75, doi: [10.1051/0004-6361/202346698](https://doi.org/10.1051/0004-6361/202346698)
- Curtis-Lake, E., Carniani, S., Cameron, A., et al. 2023, *Nature Astronomy*, 7, 622, doi: [10.1038/s41550-023-01918-w](https://doi.org/10.1038/s41550-023-01918-w)
- Daddi, E., Dickinson, M., Morrison, G., et al. 2007, *ApJ*, 670, 156, doi: [10.1086/521818](https://doi.org/10.1086/521818)
- Davé, R. 2008, *MNRAS*, 385, 147, doi: [10.1111/j.1365-2966.2008.12866.x](https://doi.org/10.1111/j.1365-2966.2008.12866.x)
- Davé, R., Finlator, K., & Oppenheimer, B. D. 2011a, *MNRAS*, 416, 1354, doi: [10.1111/j.1365-2966.2011.19132.x](https://doi.org/10.1111/j.1365-2966.2011.19132.x)
- Davé, R., Oppenheimer, B. D., & Finlator, K. 2011b, *MNRAS*, 415, 11, doi: [10.1111/j.1365-2966.2011.18680.x](https://doi.org/10.1111/j.1365-2966.2011.18680.x)
- Dayal, P., Ferrara, A., & Dunlop, J. S. 2013, *MNRAS*, 430, 2891, doi: [10.1093/mnras/stt083](https://doi.org/10.1093/mnras/stt083)
- De Rossi, M. E., Theuns, T., Font, A. S., & McCarthy, I. G. 2015, *MNRAS*, 452, 486, doi: [10.1093/mnras/stv1287](https://doi.org/10.1093/mnras/stv1287)
- D'Eugenio, F., Cameron, A. J., Scholtz, J., et al. 2024, arXiv e-prints, arXiv:2404.06531, doi: [10.48550/arXiv.2404.06531](https://doi.org/10.48550/arXiv.2404.06531)
- Diemer, B., Stevens, A. R. H., Forbes, J. C., et al. 2018, *ApJS*, 238, 33, doi: [10.3847/1538-4365/aee387](https://doi.org/10.3847/1538-4365/aee387)
- Diemer, B., Stevens, A. R. H., Lagos, C. d. P., et al. 2019, *MNRAS*, 487, 1529, doi: [10.1093/mnras/stz1323](https://doi.org/10.1093/mnras/stz1323)
- Dopita, M. A., Kewley, L. J., Heisler, C. A., & Sutherland, R. S. 2000, *ApJ*, 542, 224, doi: [10.1086/309538](https://doi.org/10.1086/309538)
- Eisenstein, D. J., Willott, C., Albers, S., et al. 2023, arXiv e-prints, arXiv:2306.02465, doi: [10.48550/arXiv.2306.02465](https://doi.org/10.48550/arXiv.2306.02465)
- Elbaz, D., Daddi, E., Le Borgne, D., et al. 2007, *A&A*, 468, 33, doi: [10.1051/0004-6361:20077525](https://doi.org/10.1051/0004-6361:20077525)
- Ellison, S. L., Patton, D. R., Simard, L., & McConnachie, A. W. 2008, *ApJL*, 672, L107, doi: [10.1086/527296](https://doi.org/10.1086/527296)
- Erb, D. K., Shapley, A. E., Pettini, M., et al. 2006a, *ApJ*, 644, 813, doi: [10.1086/503623](https://doi.org/10.1086/503623)
- Erb, D. K., Steidel, C. C., Shapley, A. E., et al. 2006b, *ApJ*, 646, 107, doi: [10.1086/504891](https://doi.org/10.1086/504891)
- Faucher-Giguère, C.-A. 2018, *MNRAS*, 473, 3717, doi: [10.1093/mnras/stx2595](https://doi.org/10.1093/mnras/stx2595)
- Feroz, F., & Hobson, M. P. 2008, *MNRAS*, 384, 449, doi: [10.1111/j.1365-2966.2007.12353.x](https://doi.org/10.1111/j.1365-2966.2007.12353.x)
- Ferruit, P., Jakobsen, P., Giardino, G., et al. 2022, *A&A*, 661, A81, doi: [10.1051/0004-6361/202142673](https://doi.org/10.1051/0004-6361/202142673)
- Figueira, M., Pollo, A., Malek, K., et al. 2022, *A&A*, 667, A29, doi: [10.1051/0004-6361/202141701](https://doi.org/10.1051/0004-6361/202141701)
- Finkelstein, S. L., Bagley, M. B., Arrabal Haro, P., et al. 2022, *ApJL*, 940, L55, doi: [10.3847/2041-8213/ac966e](https://doi.org/10.3847/2041-8213/ac966e)
- Finkelstein, S. L., Bagley, M. B., Ferguson, H. C., et al. 2023, *ApJL*, 946, L13, doi: [10.3847/2041-8213/acade4](https://doi.org/10.3847/2041-8213/acade4)
- Finlator, K., Davé, R., Papovich, C., & Hernquist, L. 2006, *ApJ*, 639, 672, doi: [10.1086/499349](https://doi.org/10.1086/499349)

- Förster Schreiber, N. M., & Wuyts, S. 2020, *ARA&A*, 58, 661, doi: [10.1146/annurev-astro-032620-021910](https://doi.org/10.1146/annurev-astro-032620-021910)
- Fujimoto, S., Arrabal Haro, P., Dickinson, M., et al. 2023, *ApJL*, 949, L25, doi: [10.3847/2041-8213/acd2d9](https://doi.org/10.3847/2041-8213/acd2d9)
- Furtak, L. J., Atek, H., Lehnert, M. D., Chevallard, J., & Charlot, S. 2021, *MNRAS*, 501, 1568, doi: [10.1093/mnras/staa3760](https://doi.org/10.1093/mnras/staa3760)
- Garcia, A. M., Torrey, P., Ellison, S. L., et al. 2024a, arXiv e-prints, arXiv:2407.06254, doi: [10.48550/arXiv.2407.06254](https://doi.org/10.48550/arXiv.2407.06254)
- Garcia, A. M., Torrey, P., Ellison, S., et al. 2024b, *MNRAS*, 531, 1398, doi: [10.1093/mnras/stae1252](https://doi.org/10.1093/mnras/stae1252)
- Garnett, D. R., & Shields, G. A. 1987, *ApJ*, 317, 82, doi: [10.1086/165257](https://doi.org/10.1086/165257)
- Grazian, A., Fontana, A., Santini, P., et al. 2015, *A&A*, 575, A96, doi: [10.1051/0004-6361/201424750](https://doi.org/10.1051/0004-6361/201424750)
- Hainline, K. N., Hviding, R. E., Rieke, M., et al. 2020, *ApJ*, 892, 125, doi: [10.3847/1538-4357/ab7dc3](https://doi.org/10.3847/1538-4357/ab7dc3)
- Hayward, C. C., & Hopkins, P. F. 2017, *MNRAS*, 465, 1682, doi: [10.1093/mnras/stw2888](https://doi.org/10.1093/mnras/stw2888)
- He, X., Wang, X., Jones, T., et al. 2024, *ApJL*, 960, L13, doi: [10.3847/2041-8213/ad12cd](https://doi.org/10.3847/2041-8213/ad12cd)
- Heintz, K. E., Brammer, G. B., Giménez-Arteaga, C., et al. 2023, *Nature Astronomy*, 7, 1517, doi: [10.1038/s41550-023-02078-7](https://doi.org/10.1038/s41550-023-02078-7)
- Heintz, K. E., Brammer, G. B., Watson, D., et al. 2024, arXiv e-prints, arXiv:2404.02211, doi: [10.48550/arXiv.2404.02211](https://doi.org/10.48550/arXiv.2404.02211)
- Henry, A., Martin, C. L., Finlator, K., & Dressler, A. 2013a, *ApJ*, 769, 148, doi: [10.1088/0004-637X/769/2/148](https://doi.org/10.1088/0004-637X/769/2/148)
- Henry, A., Scarlata, C., Domínguez, A., et al. 2013b, *ApJL*, 776, L27, doi: [10.1088/2041-8205/776/2/L27](https://doi.org/10.1088/2041-8205/776/2/L27)
- Henry, A., Rafelski, M., Sunnquist, B., et al. 2021, *ApJ*, 919, 143, doi: [10.3847/1538-4357/ac1105](https://doi.org/10.3847/1538-4357/ac1105)
- Jakobsen, P., Ferruit, P., Alves de Oliveira, C., et al. 2022, *A&A*, 661, A80, doi: [10.1051/0004-6361/202142663](https://doi.org/10.1051/0004-6361/202142663)
- Juneau, S., Bournaud, F., Charlot, S., et al. 2014, *ApJ*, 788, 88, doi: [10.1088/0004-637X/788/1/88](https://doi.org/10.1088/0004-637X/788/1/88)
- Kewley, L. J., Maier, C., Yabe, K., et al. 2013, *ApJL*, 774, L10, doi: [10.1088/2041-8205/774/1/L10](https://doi.org/10.1088/2041-8205/774/1/L10)
- Kewley, L. J., Nicholls, D. C., & Sutherland, R. S. 2019, *ARA&A*, 57, 511, doi: [10.1146/annurev-astro-081817-051832](https://doi.org/10.1146/annurev-astro-081817-051832)
- Kroupa, P. 2002, *Science*, 295, 82, doi: [10.1126/science.1067524](https://doi.org/10.1126/science.1067524)
- Langan, I., Ceverino, D., & Finlator, K. 2020, *MNRAS*, 494, 1988, doi: [10.1093/mnras/staa880](https://doi.org/10.1093/mnras/staa880)
- Langeroodi, D., & Hjorth, J. 2023, arXiv e-prints, arXiv:2307.06336, doi: [10.48550/arXiv.2307.06336](https://doi.org/10.48550/arXiv.2307.06336)
- Langeroodi, D., Hjorth, J., Chen, W., et al. 2023, *ApJ*, 957, 39, doi: [10.3847/1538-4357/acdbcl](https://doi.org/10.3847/1538-4357/acdbcl)
- Lara-López, M. A., Cepa, J., Bongiovanni, A., et al. 2010, *A&A*, 521, L53, doi: [10.1051/0004-6361/201014803](https://doi.org/10.1051/0004-6361/201014803)
- Lee, K.-S., Dey, A., Reddy, N., et al. 2011, *ApJ*, 733, 99, doi: [10.1088/0004-637X/733/2/99](https://doi.org/10.1088/0004-637X/733/2/99)
- Lee, K.-S., Ferguson, H. C., Wiklund, T., et al. 2012, *ApJ*, 752, 66, doi: [10.1088/0004-637X/752/1/66](https://doi.org/10.1088/0004-637X/752/1/66)
- Lequeux, J., Peimbert, M., Rayo, J. F., Serrano, A., & Torres-Peimbert, S. 1979, *A&A*, 80, 155
- Li, M., Cai, Z., Bian, F., et al. 2023, *ApJL*, 955, L18, doi: [10.3847/2041-8213/acf470](https://doi.org/10.3847/2041-8213/acf470)
- Lilly, S. J., Carollo, C. M., Pipino, A., Renzini, A., & Peng, Y. 2013, *ApJ*, 772, 119, doi: [10.1088/0004-637X/772/2/119](https://doi.org/10.1088/0004-637X/772/2/119)
- Lower, S., Narayanan, D., Leja, J., et al. 2020, *ApJ*, 904, 33, doi: [10.3847/1538-4357/abbfa7](https://doi.org/10.3847/1538-4357/abbfa7)
- Ma, C., Wang, K., Wang, E., et al. 2024, *ApJL*, 971, L14, doi: [10.3847/2041-8213/ad675f](https://doi.org/10.3847/2041-8213/ad675f)
- Ma, X., Hopkins, P. F., Faucher-Giguère, C.-A., et al. 2016, *MNRAS*, 456, 2140, doi: [10.1093/mnras/stv2659](https://doi.org/10.1093/mnras/stv2659)
- Madau, P., & Dickinson, M. 2014, *ARA&A*, 52, 415, doi: [10.1146/annurev-astro-081811-125615](https://doi.org/10.1146/annurev-astro-081811-125615)
- Magdis, G. E., Rigopoulou, D., Huang, J. S., & Fazio, G. G. 2010, *MNRAS*, 401, 1521, doi: [10.1111/j.1365-2966.2009.15779.x](https://doi.org/10.1111/j.1365-2966.2009.15779.x)
- Maier, C., Lilly, S. J., Ziegler, B. L., et al. 2014, *ApJ*, 792, 3, doi: [10.1088/0004-637X/792/1/3](https://doi.org/10.1088/0004-637X/792/1/3)
- Maiolino, R., Nagao, T., Grazian, A., et al. 2008a, *A&A*, 488, 463, doi: [10.1051/0004-6361:200809678](https://doi.org/10.1051/0004-6361:200809678)
- Maiolino, R., Nagao, T., Grazian, A., et al. 2008b, in *Astronomical Society of the Pacific Conference Series*, Vol. 396, Formation and Evolution of Galaxy Disks, ed. J. G. Funes & E. M. Corsini, 409
- Mannucci, F., Cresci, G., Maiolino, R., Marconi, A., & Gnerucci, A. 2010, *MNRAS*, 408, 2115, doi: [10.1111/j.1365-2966.2010.17291.x](https://doi.org/10.1111/j.1365-2966.2010.17291.x)
- Mannucci, F., Salvaterra, R., & Campisi, M. A. 2011, *MNRAS*, 414, 1263, doi: [10.1111/j.1365-2966.2011.18459.x](https://doi.org/10.1111/j.1365-2966.2011.18459.x)
- Mannucci, F., Cresci, G., Maiolino, R., et al. 2009, *MNRAS*, 398, 1915, doi: [10.1111/j.1365-2966.2009.15185.x](https://doi.org/10.1111/j.1365-2966.2009.15185.x)
- Marconcini, C., D'Eugenio, F., Maiolino, R., et al. 2024, arXiv e-prints, arXiv:2407.08616, doi: [10.48550/arXiv.2407.08616](https://doi.org/10.48550/arXiv.2407.08616)
- Marino, R. A., Rosales-Ortega, F. F., Sánchez, S. F., et al. 2013, *A&A*, 559, A114, doi: [10.1051/0004-6361/201321956](https://doi.org/10.1051/0004-6361/201321956)

- Marszewski, A., Sun, G., Faucher-Giguère, C.-A., Hayward, C. C., & Feldmann, R. 2024, *ApJL*, 967, L41, doi: [10.3847/2041-8213/ad4cee](https://doi.org/10.3847/2041-8213/ad4cee)
- Matthee, J., Mackenzie, R., Simcoe, R. A., et al. 2023, *ApJ*, 950, 67, doi: [10.3847/1538-4357/acc846](https://doi.org/10.3847/1538-4357/acc846)
- McAlpine, S., Helly, J. C., Schaller, M., et al. 2016, *Astronomy and Computing*, 15, 72, doi: [10.1016/j.ascom.2016.02.004](https://doi.org/10.1016/j.ascom.2016.02.004)
- Nakajima, K., Ouchi, M., Isole, Y., et al. 2023, *ApJS*, 269, 33, doi: [10.3847/1538-4365/acd556](https://doi.org/10.3847/1538-4365/acd556)
- Nakajima, K., Ouchi, M., Xu, Y., et al. 2022, *ApJS*, 262, 3, doi: [10.3847/1538-4365/ac7710](https://doi.org/10.3847/1538-4365/ac7710)
- Nelson, D., Pillepich, A., Springel, V., et al. 2019a, *MNRAS*, 490, 3234, doi: [10.1093/mnras/stz2306](https://doi.org/10.1093/mnras/stz2306)
- Nelson, D., Springel, V., Pillepich, A., et al. 2019b, *Computational Astrophysics and Cosmology*, 6, 2, doi: [10.1186/s40668-019-0028-x](https://doi.org/10.1186/s40668-019-0028-x)
- Noeske, K. G., Weiner, B. J., Faber, S. M., et al. 2007, *ApJL*, 660, L43, doi: [10.1086/517926](https://doi.org/10.1086/517926)
- Oke, J. B., & Gunn, J. E. 1983, *ApJ*, 266, 713, doi: [10.1086/160817](https://doi.org/10.1086/160817)
- Onodera, M., Carollo, C. M., Lilly, S., et al. 2016, *ApJ*, 822, 42, doi: [10.3847/0004-637X/822/1/42](https://doi.org/10.3847/0004-637X/822/1/42)
- Osterbrock, D. E., & Ferland, G. J. 2006, *Astrophysics of gaseous nebulae and active galactic nuclei*
- Pallottini, A., Ferrara, A., Gallerani, S., et al. 2022, *MNRAS*, 513, 5621, doi: [10.1093/mnras/stac1281](https://doi.org/10.1093/mnras/stac1281)
- Pannella, M., Carilli, C. L., Daddi, E., et al. 2009, *ApJL*, 698, L116, doi: [10.1088/0004-637X/698/2/L116](https://doi.org/10.1088/0004-637X/698/2/L116)
- Pettini, M., & Pagel, B. E. J. 2004, *MNRAS*, 348, L59, doi: [10.1111/j.1365-2966.2004.07591.x](https://doi.org/10.1111/j.1365-2966.2004.07591.x)
- Pistis, F., Pollo, A., Figueira, M., et al. 2024, *A&A*, 683, A203, doi: [10.1051/0004-6361/202346943](https://doi.org/10.1051/0004-6361/202346943)
- Planck Collaboration, Aghanim, N., Akrami, Y., et al. 2020, *A&A*, 641, A6, doi: [10.1051/0004-6361/201833910](https://doi.org/10.1051/0004-6361/201833910)
- Pontoppidan, K. M., Barrientes, J., Blome, C., et al. 2022, *ApJL*, 936, L14, doi: [10.3847/2041-8213/ac8a4e](https://doi.org/10.3847/2041-8213/ac8a4e)
- Popesso, P., Concas, A., Cresci, G., et al. 2023, *MNRAS*, 519, 1526, doi: [10.1093/mnras/stac3214](https://doi.org/10.1093/mnras/stac3214)
- Reddy, N. A., Steidel, C. C., Fadda, D., et al. 2006, *ApJ*, 644, 792, doi: [10.1086/503739](https://doi.org/10.1086/503739)
- Roberts-Borsani, G., Treu, T., Shapley, A., et al. 2024, *arXiv e-prints*, arXiv:2403.07103, doi: [10.48550/arXiv.2403.07103](https://doi.org/10.48550/arXiv.2403.07103)
- Robertson, B. E. 2022, *ARA&A*, 60, 121, doi: [10.1146/annurev-astro-120221-044656](https://doi.org/10.1146/annurev-astro-120221-044656)
- Salim, S., Lee, J. C., Ly, C., et al. 2014, *ApJ*, 797, 126, doi: [10.1088/0004-637X/797/2/126](https://doi.org/10.1088/0004-637X/797/2/126)
- Salmon, B., Papovich, C., Finkelstein, S. L., et al. 2015, *ApJ*, 799, 183, doi: [10.1088/0004-637X/799/2/183](https://doi.org/10.1088/0004-637X/799/2/183)
- Sánchez, S. F., Barrera-Ballesteros, J. K., Sánchez-Menguiano, L., et al. 2017, *MNRAS*, 469, 2121, doi: [10.1093/mnras/stx808](https://doi.org/10.1093/mnras/stx808)
- Sanders, R. L., Shapley, A. E., Topping, M. W., Reddy, N. A., & Brammer, G. B. 2024, *ApJ*, 962, 24, doi: [10.3847/1538-4357/ad15fc](https://doi.org/10.3847/1538-4357/ad15fc)
- Sanders, R. L., Shapley, A. E., Kriek, M., et al. 2015, *ApJ*, 799, 138, doi: [10.1088/0004-637X/799/2/138](https://doi.org/10.1088/0004-637X/799/2/138)
- Sanders, R. L., Shapley, A. E., Jones, T., et al. 2021, *ApJ*, 914, 19, doi: [10.3847/1538-4357/abf4c1](https://doi.org/10.3847/1538-4357/abf4c1)
- Santini, P., Fontana, A., Castellano, M., et al. 2017, *ApJ*, 847, 76, doi: [10.3847/1538-4357/aa8874](https://doi.org/10.3847/1538-4357/aa8874)
- Sarkar, A., Ferland, G. J., Chatzikos, M., et al. 2021, *ApJ*, 907, 12, doi: [10.3847/1538-4357/abcaa6](https://doi.org/10.3847/1538-4357/abcaa6)
- Shapley, A. E., Reddy, N. A., Sanders, R. L., Topping, M. W., & Brammer, G. B. 2023, *ApJL*, 950, L1, doi: [10.3847/2041-8213/acd939](https://doi.org/10.3847/2041-8213/acd939)
- Sparre, M., Hayward, C. C., Feldmann, R., et al. 2017, *MNRAS*, 466, 88, doi: [10.1093/mnras/stw3011](https://doi.org/10.1093/mnras/stw3011)
- Speagle, J. S., Steinhardt, C. L., Capak, P. L., & Silverman, J. D. 2014, *ApJS*, 214, 15, doi: [10.1088/0067-0049/214/2/15](https://doi.org/10.1088/0067-0049/214/2/15)
- Springel, V., Pakmor, R., Pillepich, A., et al. 2018, *MNRAS*, 475, 676, doi: [10.1093/mnras/stx3304](https://doi.org/10.1093/mnras/stx3304)
- Stark, D. P., Schenker, M. A., Ellis, R., et al. 2013, *ApJ*, 763, 129, doi: [10.1088/0004-637X/763/2/129](https://doi.org/10.1088/0004-637X/763/2/129)
- Steidel, C. C., Rudie, G. C., Strom, A. L., et al. 2014, *ApJ*, 795, 165, doi: [10.1088/0004-637X/795/2/165](https://doi.org/10.1088/0004-637X/795/2/165)
- Steinhardt, C. L., Speagle, J. S., Capak, P., et al. 2014, *ApJL*, 791, L25, doi: [10.1088/2041-8205/791/2/L25](https://doi.org/10.1088/2041-8205/791/2/L25)
- Storey, P. J., & Zeppen, C. J. 2000, *MNRAS*, 312, 813, doi: [10.1046/j.1365-8711.2000.03184.x](https://doi.org/10.1046/j.1365-8711.2000.03184.x)
- Suresh, J., Bird, S., Vogelsberger, M., et al. 2015, *MNRAS*, 448, 895, doi: [10.1093/mnras/stu2762](https://doi.org/10.1093/mnras/stu2762)
- Torrey, P., Vogelsberger, M., Marinacci, F., et al. 2019, *MNRAS*, 484, 5587, doi: [10.1093/mnras/stz243](https://doi.org/10.1093/mnras/stz243)
- Tremonti, C. A., Heckman, T. M., Kauffmann, G., et al. 2004, *ApJ*, 613, 898, doi: [10.1086/423264](https://doi.org/10.1086/423264)
- Treu, T., Roberts-Borsani, G., Bradac, M., et al. 2022, *ApJ*, 935, 110, doi: [10.3847/1538-4357/ac8158](https://doi.org/10.3847/1538-4357/ac8158)
- Troncoso, P., Maiolino, R., Sommariva, V., et al. 2014, *A&A*, 563, A58, doi: [10.1051/0004-6361/201322099](https://doi.org/10.1051/0004-6361/201322099)
- Ucci, G., Dayal, P., Hutter, A., et al. 2023, *MNRAS*, 518, 3557, doi: [10.1093/mnras/stac2654](https://doi.org/10.1093/mnras/stac2654)
- Venturi, G., Carniani, S., Parlanti, E., et al. 2024, *arXiv e-prints*, arXiv:2403.03977, doi: [10.48550/arXiv.2403.03977](https://doi.org/10.48550/arXiv.2403.03977)
- Vogelsberger, M., Marinacci, F., Torrey, P., & Puchwein, E. 2020, *Nature Reviews Physics*, 2, 42, doi: [10.1038/s42254-019-0127-2](https://doi.org/10.1038/s42254-019-0127-2)

- Vogelsberger, M., Genel, S., Springel, V., et al. 2014a, *Nature*, 509, 177, doi: [10.1038/nature13316](https://doi.org/10.1038/nature13316)
- . 2014b, *MNRAS*, 444, 1518, doi: [10.1093/mnras/stu1536](https://doi.org/10.1093/mnras/stu1536)
- Wang, X., Cheng, C., Ge, J., et al. 2024, *ApJL*, 967, L42, doi: [10.3847/2041-8213/ad4ced](https://doi.org/10.3847/2041-8213/ad4ced)
- Wilkins, S. M., Vijayan, A. P., Lovell, C. C., et al. 2023, *MNRAS*, 519, 3118, doi: [10.1093/mnras/stac3280](https://doi.org/10.1093/mnras/stac3280)
- York, D. G., Adelman, J., Anderson, John E., J., et al. 2000, *AJ*, 120, 1579, doi: [10.1086/301513](https://doi.org/10.1086/301513)
- Zahid, H. J., Bresolin, F., Kewley, L. J., Coil, A. L., & Davé, R. 2012, *ApJ*, 750, 120, doi: [10.1088/0004-637X/750/2/120](https://doi.org/10.1088/0004-637X/750/2/120)
- Zahid, H. J., Geller, M. J., Kewley, L. J., et al. 2013, *ApJL*, 771, L19, doi: [10.1088/2041-8205/771/2/L19](https://doi.org/10.1088/2041-8205/771/2/L19)
- Zahid, H. J., Kewley, L. J., & Bresolin, F. 2011, *ApJ*, 730, 137, doi: [10.1088/0004-637X/730/2/137](https://doi.org/10.1088/0004-637X/730/2/137)
- Zaritsky, D., Kennicutt, Robert C., J., & Huchra, J. P. 1994, *ApJ*, 420, 87, doi: [10.1086/173544](https://doi.org/10.1086/173544)

## APPENDIX

**Table 2.** GOODS-S and GOODS-N JWST/NIRSpec Sample of Galaxies Analysed in this Paper (D'Eugenio et al. 2024).

NIRSpec ID	RA	Dec	$z$	$\log(M_*/M_\odot)$	$\log(\text{SFR}_{\text{H}\beta})$	$12+\log(\text{O}/\text{H})$
42453	53.1173859	-27.8033791	4.46	$7.67 \pm 0.11$	$0.01 \pm 0.12$	$7.52 \pm 0.20$
103483	53.188310688	-27.81283361	5.27	$7.09 \pm 0.09$	$0.66 \pm 0.11$	$7.34 \pm 0.16$
10004736	53.1640716	-27.8191086	4.03	$8.57 \pm 0.04$	$-0.10 \pm 0.11$	$8.48 \pm 0.01$
110	189.146378721	62.21550823	4.07	$9.45 \pm 0.02$	$1.14 \pm 0.01$	$8.29 \pm 0.01$
604	189.117202094	62.2214337	4.16	$8.62 \pm 0.03$	$0.64 \pm 0.05$	$8.22 \pm 0.07$
607	189.116947265	62.22207876	5.19	$8.32 \pm 0.03$	$0.94 \pm 0.04$	$7.87 \pm 0.05$
666	189.113413603	62.2276564	4.92	$8.39 \pm 0.04$	$0.64 \pm 0.14$	$7.70 \pm 0.11$
795	189.191792532	62.24204531	4.79	$9.32 \pm 0.03$	$0.93 \pm 0.07$	$8.42 \pm 0.05$
834	189.09701079	62.24698089	4.91	$8.42 \pm 0.05$	$0.67 \pm 0.13$	$7.34 \pm 0.16$
896	189.082651931	62.25247723	6.77	$8.87 \pm 0.02$	$1.38 \pm 0.02$	$8.00 \pm 0.03$
902	189.193276303	62.25372707	4.07	$8.51 \pm 0.02$	$0.95 \pm 0.02$	$7.87 \pm 0.05$
910	189.113442988	62.25480338	4.42	$8.62 \pm 0.02$	$0.53 \pm 0.05$	$7.59 \pm 0.07$
917	189.080143561	62.25539861	4.41	$8.61 \pm 0.02$	$0.53 \pm 0.05$	$8.13 \pm 0.04$
964	189.13723537	62.26063625	5.61	$8.10 \pm 0.03$	$1.09 \pm 0.04$	$7.85 \pm 0.04$
971	189.130932109	62.26199976	4.43	$9.28 \pm 0.03$	$0.92 \pm 0.05$	$8.33 \pm 0.05$
993	189.081903696	62.26492219	4.18	$7.89 \pm 0.04$	$0.46 \pm 0.08$	$8.00 \pm 0.10$
1044	189.111041015	62.27190179	4.04	$8.16 \pm 0.03$	$0.51 \pm 0.04$	$7.78 \pm 0.08$
1129	189.179752709	62.28238705	7.09	$8.15 \pm 0.03$	$1.27 \pm 0.04$	$7.81 \pm 0.08$
1139	189.176550776	62.28372336	4.16	$8.17 \pm 0.08$	$0.08 \pm 0.14$	$7.76 \pm 0.09$
1560	189.100309169	62.23085249	5.20	$8.24 \pm 0.03$	$0.86 \pm 0.04$	$7.78 \pm 0.08$
1674	189.131144715	62.27035136	4.05	$8.52 \pm 0.01$	$0.53 \pm 0.05$	$7.77 \pm 0.09$
1926	189.140718886	62.27724124	4.04	$9.71 \pm 0.03$	$0.65 \pm 0.05$	$8.40 \pm 0.04$
1931	189.069641344	62.28101917	7.04	$8.05 \pm 0.07$	$0.89 \pm 0.06$	$7.59 \pm 0.09$
1948	189.177312132	62.29105785	6.74	$8.34 \pm 0.07$	$0.82 \pm 0.04$	$7.76 \pm 0.09$
2000	189.175947335	62.31153443	5.66	$8.66 \pm 0.01$	$0.81 \pm 0.07$	$7.69 \pm 0.12$
2113	189.170329427	62.22949872	6.72	$7.71 \pm 0.11$	$1.02 \pm 0.05$	$7.93 \pm 0.03$
3012	189.120110053	62.30436157	5.27	$8.93 \pm 0.06$	$0.57 \pm 0.15$	$8.34 \pm 0.13$
3608	189.117937758	62.2355185	5.28	$7.53 \pm 0.03$	$0.86 \pm 0.02$	$7.71 \pm 0.05$
4545	189.185252674	62.23876092	4.05	$8.08 \pm 0.08$	$-0.24 \pm 0.14$	$8.15 \pm 0.12$
7351	189.108182935	62.24714628	6.05	$8.30 \pm 0.04$	$0.84 \pm 0.07$	$8.00 \pm 0.04$
12067	189.207450251	62.26445323	4.07	$8.50 \pm 0.03$	$0.45 \pm 0.05$	$8.19 \pm 0.07$
13410	189.188837292	62.2699137	5.02	$8.78 \pm 0.06$	$0.61 \pm 0.06$	$8.29 \pm 0.07$
16553	189.143602845	62.28054547	4.39	$8.47 \pm 0.02$	$0.81 \pm 0.02$	$8.00 \pm 0.10$
17722	189.108883186	62.28421706	4.94	$8.24 \pm 0.02$	$0.75 \pm 0.05$	$7.83 \pm 0.05$
24819	189.136473583	62.22340297	7.14	$9.14 \pm 0.03$	$0.93 \pm 0.04$	$8.40 \pm 0.03$
25356	189.147811293	62.23045386	4.42	$9.08 \pm 0.03$	$0.36 \pm 0.06$	$8.23 \pm 0.07$
27003	189.014595403	62.26820484	5.60	$8.82 \pm 0.03$	$1.02 \pm 0.04$	$7.81 \pm 0.07$
28174	189.227700921	62.25176394	4.41	$9.07 \pm 0.04$	$0.93 \pm 0.01$	$8.17 \pm 0.03$
28229	189.225841987	62.25193981	4.41	$8.78 \pm 0.10$	$0.45 \pm 0.07$	$8.20 \pm 0.04$
28746	189.17607762	62.2563246	4.43	$8.83 \pm 0.01$	$0.98 \pm 0.02$	$8.36 \pm 0.02$
32944	189.089677913	62.3048876	4.29	$9.73 \pm 0.03$	$0.68 \pm 0.05$	$8.45 \pm 0.03$
38849	189.155065954	62.25900074	4.42	$7.82 \pm 0.06$	$0.27 \pm 0.10$	$8.14 \pm 0.11$

**Table 3.** Continued.

NIRSpec ID	RA	Dec	$z$	$\log(M_*/M_\odot)$	$\log(\text{SFR}_{\text{H}\beta})$	$12+\log(\text{O}/\text{H})$
52923	189.286013502	62.19204378	4.02	$8.11 \pm 0.01$	$0.38 \pm 0.04$	$8.00 \pm 0.02$
58561	189.221830211	62.20735743	6.55	$7.80 \pm 0.03$	$0.92 \pm 0.03$	$7.74 \pm 0.06$
59156	189.306169277	62.20920468	5.23	$8.78 \pm 0.06$	$0.81 \pm 0.05$	$8.16 \pm 0.03$
62309	189.248977223	62.21835017	5.17	$7.64 \pm 0.03$	$0.74 \pm 0.04$	$7.88 \pm 0.03$
71093	189.275721336	62.16168901	5.05	$9.24 \pm 0.02$	$0.98 \pm 0.03$	$8.43 \pm 0.02$
73488	189.197395939	62.17723313	4.14	$9.50 \pm 0.01$	$0.83 \pm 0.02$	$7.71 \pm 0.03$
79349	189.20968225	62.20725204	5.19	$7.84 \pm 0.03$	$0.83 \pm 0.02$	$8.00 \pm 0.10$
80185	189.14847252	62.21165963	5.49	$7.80 \pm 0.03$	$0.66 \pm 0.05$	$7.81 \pm 0.07$
80391	189.194218105	62.21250554	4.63	$8.65 \pm 0.05$	$0.36 \pm 0.13$	$7.78 \pm 0.08$
82830	189.237876124	62.2340822	5.80	$8.09 \pm 0.03$	$0.60 \pm 0.07$	$7.70 \pm 0.12$
10000885	189.270594	62.25156684	4.42	$8.90 \pm 0.02$	$1.05 \pm 0.04$	$8.20 \pm 0.06$

**Table 4.** JWST/NIRSpec Sample of Galaxies from Primal Survey (Heintz et al. 2024)

NIRSpec ID	RA	Dec	$z$	$\log(M_*/M_\odot)$	$\log(\text{SFR}_{\text{H}\beta})$	$12+\log(\text{O}/\text{H})$
9457	53.17324	-27.795674	6.00	$8.66 \pm 0.03$	$0.76 \pm 0.06$	$8.01 \pm 0.09$
50010	189.2881531	62.1837804	6.04	$8.00 \pm 0.12$	$0.55 \pm 0.11$	$7.99 \pm 0.15$
13887	53.1958751	-27.7684324	6.05	$8.11 \pm 0.08$	$0.62 \pm 0.09$	$7.90 \pm 0.10$
99302	53.125818	-27.818228	6.07	$7.79 \pm 0.08$	$0.06 \pm 0.05$	$8.20 \pm 0.13$
617	214.860024	52.898125	6.23	$7.11 \pm 0.04$	$0.60 \pm 0.06$	$7.70 \pm 0.08$
15265	53.0831133	-27.786351	6.27	$7.66 \pm 0.04$	$1.03 \pm 0.04$	$7.99 \pm 0.15$
42988	53.0906811	-27.7442159	6.27	$8.51 \pm 0.04$	$0.81 \pm 0.06$	$8.03 \pm 0.20$
1817	189.3963575	62.2301725	6.32	$8.30 \pm 0.10$	$0.78 \pm 0.08$	$7.73 \pm 0.12$
106197	53.131047	-27.8090823	6.34	$7.46 \pm 1.30$	$-0.03 \pm 0.07$	$7.57 \pm 0.09$
662	214.877883	52.897675	6.54	$7.20 \pm 0.13$	$0.75 \pm 0.04$	$7.27 \pm 0.10$
449	214.940489	52.932556	7.55	$7.60 \pm 0.20$	$0.64 \pm 0.06$	$7.70 \pm 0.07$
10038687	189.2030733	62.1439285	7.57	$8.30 \pm 0.20$	$0.51 \pm 0.21$	$7.44 \pm 0.12$
9074	53.0863067	-27.8239613	7.61	$8.10 \pm 0.10$	$1.12 \pm 0.08$	$8.00 \pm 0.10$
12637	53.133469	-27.760373	7.66	$8.60 \pm 0.03$	$1.30 \pm 0.02$	$8.00 \pm 0.10$
3626	53.0873836	-27.8603113	7.96	$9.37 \pm 0.14$	$1.37 \pm 0.16$	$7.50 \pm 0.22$
20198852	53.1077607	-27.812944	8.27	$7.60 \pm 0.10$	$0.28 \pm 0.06$	$7.30 \pm 0.10$
20213084	53.1589064	-27.765076	8.49	$8.09 \pm 0.03$	$0.79 \pm 0.03$	$7.90 \pm 0.13$
20100293	53.1687381	-27.8169753	8.75	$8.00 \pm 0.20$	$0.20 \pm 0.11$	$7.55 \pm 0.15$
28	214.938642	52.911749	8.76	$8.70 \pm 0.10$	$1.31 \pm 0.03$	$7.95 \pm 0.10$
20110306	53.1691329	-27.8029208	8.92	$7.80 \pm 0.10$	$-0.12 \pm 0.19$	$8.07 \pm 0.14$
10278	53.13916658	-27.8484843	9.06	$9.10 \pm 0.10$	$1.16 \pm 0.11$	$7.87 \pm 0.12$
3990	189.0169954	62.2415817	9.38	$8.65 \pm 0.04$	$1.75 \pm 0.03$	$7.30 \pm 0.12$

**Table 5.** JWST Sample of Galaxies from literature

Target	RA	Dec	$z$	$\log(M_*/M_\odot)$	$\log(\text{SFR}_{\text{H}\beta})$	$12+\log(\text{O}/\text{H})$	Source
A2744-YD4	3.60375	-30.38225	7.88	$8.69 \pm 0.17$	$0.61 \pm 0.04$	$8.19 \pm 0.13$	Venturi et al. (2024)
BDF-3299-a	337.05	-35.166	7.11	$7.90 \pm 0.19$	$0.51 \pm 0.01$	$7.68 \pm 0.09$	Venturi et al. (2024)
COSMOS24108-a	150.1972	2.47865	6.36	$9.29 \pm 0.08$	$0.56 \pm 0.04$	$8.20 \pm 0.05$	Venturi et al. (2024)
RX2129-z8HeII	322.416266	0.099675	8.16	$7.75 \pm 0.06$	$0.94 \pm 0.07$	$7.63 \pm 0.14$	Wang et al. (2024)
MACS1149-JD1	177.389945	22.412722	9.11	$8.47 \pm 0.05$	$0.40 \pm 0.06$	$8.00 \pm 0.18$	Marconcini et al. (2024)